PHYSICAL REVIEW RESEARCH **5**, 013224 (2023)

Mapping state transition susceptibility in quantum annealing

Elijah Pelofske [*]
Los Alamos National Laboratory, CCS-3, Los Alamos, New Mexico 87545, USA

(Received 25 October 2022; accepted 28 February 2023; published 31 March 2023)

Quantum annealing is a novel type of analog computation that aims to use quantum-mechanical fluctuations to search for optimal solutions for Ising problems. Quantum annealing in the transverse field Ising model, implemented on D-Wave devices, works by applying a time-dependent transverse field, which puts all qubits into a uniform state of superposition, and then applying a Hamiltonian over time, which describes a user-programed Ising problem. We present a method that utilizes two control features of D-Wave quantum annealers, namely reverse annealing and an *h*-gain schedule, to quantify the susceptibility, or the distance, between two classical states of an Ising problem. The starting state is encoded using reverse annealing, and the second state is encoded on the linear terms of a problem Hamiltonian. An *h*-gain schedule is specified, which incrementally increases the strength of the linear terms, thus allowing a quantification of the *h*-gain strength required to transition the anneal into a specific state at the final measurement. Because of the nature of quantum annealing, the state tends towards global minima, and therefore we restrict the second classical state to a minimum solution of the given Ising problem. This susceptibility mapping, when enumerated across all initial states, shows in detail the behavior of the quantum annealer during reverse annealing. The procedure is experimentally demonstrated on three small test Ising models which were embedded in parallel on the D-Wave Advantage_system4.1. Analysis of the state transition mapping shows detailed characteristics of the reverse annealing process, including intermediate state transition paths, which are visually represented as state transition networks.

DOI: 10.1103/PhysRevResearch.5.013224

I. INTRODUCTION

Quantum annealing in the transverse field Ising model was proposed as a novel analog computation model that utilizes quantum fluctuations in order to search for optimal solutions of combinatorial optimization problems [1–6]. Adiabatic quantum computing is an ideal computation that is entirely isolated from the environment and slowly evolves the Hamiltonian [7]. Adiabatic quantum computing (AQC) is of interest because it is equivalent to circuit model quantum computing. Quantum annealing (QA) is a practical heuristic implementation of adiabatic quantum computing [7] where the coherence times are small [8], the system is not perfectly isolated from the environment, the variable connectivity is limited, and the time evolution is not necessarily slow. Quantum annealing has been implemented in hardware in a variety of contexts [8–11], and D-Wave system quantum annealing hardware is currently available as a cloud computing resource. D-Wave quantum annealers are implemented via typically sparse hardware graphs of superconducting flux qubits. Quantum annealing has been used as an experimental physics simulation tool [12–16] and as a computer to sample a wide variety of optimization problems [17–20] including, to name specific problem types, the graph coloring problem [21,22] semiprime factorization [23–28] the traveling salesperson problem [29,30], air traffic management [31], maximum clique [32–34], graph partitioning [35,36], boolean tensor networks [37–39], community detection [40], spanning trees [41], fault detection [42], and maximum cut [43,44]. Following with the theme of sampling optimization problems that are of interest for many possible applications, there have been numerous studies developing methods to improve the capabilities of modern quantum annealers using different parameter tuning techniques and algorithms [44–51]. Overall, quantum annealing, and in particular the cloud based D-Wave systems quantum annealers, are an active topic of study because of the potential heuristic capability of quantum annealing to sample optimization problems of interest in the NISQ-era [52] where hardware error rates and limited hardware connectivity [53–55] prohibit more exact computation. For D-Wave quantum annealers, the Hamiltonian that is implemented in hardware can be represented in Eq. (1) as a sum of the initial transverse field Hamiltonian and the user-encoded Hamiltonian,

$$H_{\text{Ising}} = -\frac{A(s)}{2}\left(\sum_i \hat{\sigma}_x^{(i)}\right) + \frac{B(s)}{2}\left(\sum_i h_i \hat{\sigma}_z^{(i)} + \sum_{i>j} J_{i,j}\hat{\sigma}_z^{(i)}\hat{\sigma}_z^{(j)}\right), \quad (1)$$

---

[*] epelofske@lanl.gov

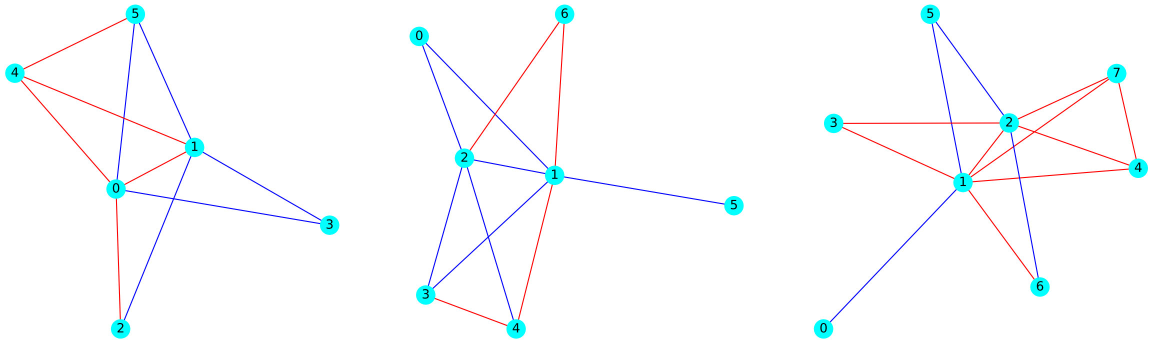

FIG. 1. The logical N_6 Ising, N_7, and N_8 in order from left to right. Quadratic weights of $+1$ are encoded as blue edges in these problem graphs, and quadratic weights of -1 are encoded as red edges in these problem graphs. The N_6 Ising has four ground states (optimal solutions), N_7 has two ground states, and N_8 has eight ground states. All linear terms are set to 0. The variable indices are drawn on the node labels. Each of these Ising models are subgraphs of the Pegasus graph topology.

where $\hat{\sigma}_{x,z}$ are Pauli matrices operating on qubit i. $h_i \in \mathbb{R}$ are the qubit biases, and $J_{i,j} \in \mathbb{R}$ are the coupling strengths. D-Wave quantum annealers also allow users to change many parameters of the anneal beyond the problem Ising that is mapped to the device. For example, the users can modify the annealing schedule that defines where the anneal fraction s is at each time step in the anneal; in normal forward annealing, the points of the anneal schedule are defined as a linear interpolation from $s = 0$ at the start of the anneal and $s = 1$ at the end of the anneal [56]. Another relevant parameter that the user of cloud-based D-Wave quantum annealers can specify is the *annealing time* which specifies the anneal duration in microseconds (for the D-Wave `Advantage_system4.1`, for example, the annealing times can be in a range from 0.5 to 2000). Equation (2) defines the problem Hamiltonian that is minimized during quantum annealing as a variable assignment problem,

$$H(x_1, \dots, x_n) = \sum_{i}^{n} h_i x_i + \sum_{i>j} J_{i,j} x_i x_j. \tag{2}$$

The linear weights $h_i \in \mathbb{R}$ and the quadratic couplers $J_{ij} \in \mathbb{R}$ define the discrete optimization problem, where the goal is to find the assignment of unknown binary variables x_i, $i \in \{1, \dots, n\}$ that minimizes Eq. (2). Equation (2) is called a Quadratic Unconstrained Binary Optimization problem (*QUBO*) problem if $x_i \in \{0, 1\}$, and an *Ising* problem if $x_i \in \{-1, +1\}$, where $i \in \{1, \dots, n\}$. The reason that quantum annealing can be applied to so many different problem types, including NP-Hard problems, is because they can be formulated as Ising models [57], or equivalently QUBOs [58,59], which can be mapped to a problem Hamiltonian of the form of Eq. (2).

Alongside expanding its possible application domains, understanding the dynamics of how quantum annealers sample problems has been a subject of research [60–64]. For example, one of the examples of a notable property of quantum annealing in the transverse field Ising model is that it does not sample ground states fairly for optimization problems which have multiple optimal solutions [65–72]. Fairly sampling optimal solutions, while not always necessary when solving optimization problems, is important for a variety of applications [73–81].

In this article, we present a state transition susceptibility mapping methodology where a quantification can be made of the susceptibility of transitioning between two classical states in a quantum annealer, which can then be enumerated across all possible initial states for small Ising models. This state mapping is accomplished by specifying an initial classical state as the starting point of the anneal (this is accomplished using *reverse annealing*), and h-gain state encoding guides the anneal towards a specific intended classical ground state. This measure can be regarded as a type of susceptibility because it is measuring the response to an applied magnetic field during the quantum annealing process. These data are then analyzed using several different metrics which show correlations between initial state energy and hamming distance proportions. The data are then further characterized by creating state transition networks to show intermediate states. The results show that there are some initial states that are significantly more susceptible to being moved into an intended ground state, but are not necessarily near the ground state in terms of energy. The results are also analyzed to determine if they have a biased state transition susceptibility towards some ground states, and if that correlates to unfair sampling in forward annealing.

All raw data from the experiments are publicly available datasets [82–85].

II. METHODS

In this section, we outline the experimental methods used to map the susceptibility from input states to ground states of small test Ising models. First, in Sec. II A we outline the three Ising problems that will be investigated. In Sec. II B, we present the settings and methods used to encode the initial state and the intended ground state of the Ising models. In Sec. II C, the different metrics that the results will be analyzed with are defined. All figures generated in this article use the python packages MATPLOTLIB [86,87] and NETWORKX [88].

A. Problem Ising models and hardware embedding

Figure 1 defines the three problem Ising models we will investigate. Importantly, these three Ising models are natively embeddable onto the D-Wave Pegasus Quantum Processing Unit (QPU) topology [55,89,90]. This allows for these small

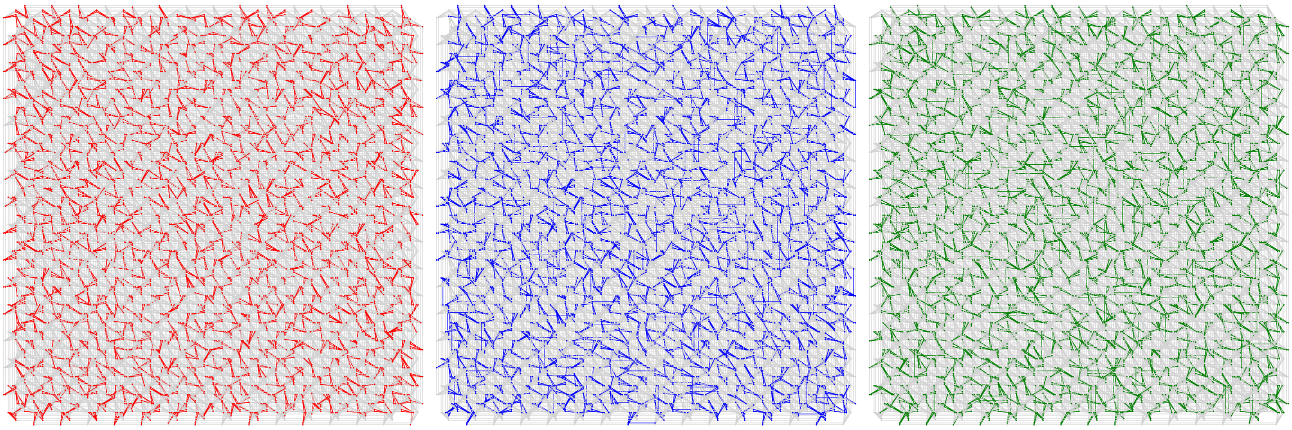

FIG. 2. Test Ising models embedded in parallel onto the hardware connectivity graph of Advantage_system4.1. The N_6 Ising is embedded 722 times (left). The N_7 Ising is embedded 625 times (middle). The N_8 Ising is embedded 525 times (right). The nodes and edges used in the hardware graph embeddings are colored red (left), blue (middle), and green (right), and unused qubits and couplers are colored with high-transparency gray. The Advantage_system4.1 device has a Pegasus P_{16} topology, however it also has some missing hardware components (qubits and couplers) which are unintentional manufacturing defects, therefore these parallel (or *tiled*) embeddings must account for these hardware defects.

Ising models to be repeatedly embedded onto the chip connectivity, which allows us to execute a large sample size of these small Ising models *in parallel* during the same annealing cycle—i.e., *parallel quantum annealing* [32,39]. These parallel embeddings are also referred to as *tiling* [91]. Embedding many problem instances onto the hardware not only ensures that robust statistics of the problem will be gathered, but it also aims to average out any specific biases that may exist for specific groups of qubits. Not using minor-embedding also mitigates the additional potential problems that can come with minor embedding [92], including resolving chain breaks [34,93] and the ferromagnetic coupling chain strength dominating the programed energy scale on the chip [94]. All experiments use the D-Wave Advantage_system4.1; Fig. 2 shows these three Ising models embedded onto the Advantage_system4.1 connectivity at least several hundred times using the minorminer heuristic minor embedding tool [95]. These test Ising models were selected for several reasons.

(i) They match the native connectivity of the Pegasus graph, which means that minor embedding will not be required in order to execute these Ising models on D-Wave Advantage_system4.1.

(ii) They have multiple optimal solutions, which allows us to examine any differences, or similarities, in the behavior of the *h*-gain response curves for the different ground states.

(iii) They are simple random spin glasses, which are typical for test problems on quantum annealers [67,96–98], and in general this class of problem is NP-Hard [99].

(iv) They are small enough that we can easily compute their optimal solutions and we can also enumerate over all possible initial states with the reverse annealing and *h*-gain state encoding methods.

(v) Linear terms are intentionally not included on the problem Ising so that the *h-gain state encoding* can be utilized.

Because these Ising models are sufficiently small, it is possible to enumerate over all possible solutions of the variable assignment problem $\{+1, -1\}$ and determine which states are the optimal solutions. These types of Ising problems (meaning edge coefficients with a weight of either 1 or -1 and there no linear terms) naturally will have complementary ground states, meaning that there are always at least two optimal solutions and they will be complements of each other. Here we provide these Ising optimal solutions:

(i) The N_6 Ising has exactly four optimal solutions, each with an energy of -6. These optimal variable assignments are $[-1, -1, -1, +1, -1, +1]$, $[-1, -1, +1, +1, -1, +1]$, $[+1, +1, -1, -1, +1, -1]$, $[+1, +1, +1, -1, +1, -1]$.

(ii) The N_7 Ising has exactly two optimal solutions, each with an energy of -7. These optimal variable assignments are $[-1, +1, +1, -1, -1, -1, +1]$, $[+1, -1, -1, +1, +1, +1, -1]$.

(iii) The N_8 Ising has exactly eight optimal solutions, each with an energy of -11. These optimal variable assignments are $[-1, +1, -1, +1, +1, -1, -1, +1]$, $[-1, +1, -1, +1, +1, -1, +1, +1]$, $[-1, +1, +1, -1, -1, -1, +1, +1]$, $[-1, +1, +1, -1, +1, -1, +1, +1]$, $[+1, -1, -1, +1, -1, +1, -1, -1]$, $[+1, -1, -1, +1, +1, +1, -1, -1]$, $[+1, -1, +1, -1, -1, +1, -1, -1]$, $[+1, -1, +1, -1, -1, +1, +1, -1]$.

B. State encoding methods

The *h*_gain_schedule parameter on D-Wave quantum annealers works by introducing a time-dependent function $g(t)$ to the linear terms of the problem Hamiltonian, resulting in a modified version of Eq. (1),

$$H_{\text{Ising}} = -\frac{A(s)}{2}\left(\sum_i \hat{\sigma}_x^{(i)}\right) + \frac{B(s)}{2}\left(g(t)\sum_i h_i \hat{\sigma}_z^{(i)} + \sum_{i>j} J_{i,j}\hat{\sigma}_z^{(i)}\hat{\sigma}_z^{(j)}\right). \quad (3)$$

The h-gain feature of D-Wave quantum annealers has been used before in a variety of contexts [12,43,60,100,101]. The h-gain feature could also be used for other interesting simulation methods such as implementing adiabatic reverse annealing [102,103]. The h-gain field allows the user to program a longitudinal magnetic field into the system according to a specific schedule, meaning that it can vary over time. The h-gain encoding of the ground-state solutions involves specifying the linear weights of the Ising as the complements (multiply all variables by -1) of the ground state. Then we also specify the h_gain_schedule (which starts out at 0 strength). More details of this implementation can be found in Ref. [43]. For simplicity, the Ising models we consider in this study do not have linear terms, however it is important to note that by introducing an additional slack variable (which may require minor-embedding depending on the problem) one can still utilize this h-gain encoding method for other problems. For consistency, in the article when referring to this specific encoding method, the term *h-gain state encoding* will be used.

The h_gain_schedule is defined to be `[[0.0, 0], [0.05, 0], [0.1, h], [99.1, h], [99.15, 0], [100, 0]]` where the first coordinate is time in microseconds, and the second coordinate is the applied factor by which the linear terms are multiplied [i.e., this schedule defines the function $g(t)$]. The parameter h is varied from 0.1 to 3 in steps of 0.1; 3 is the maximum h-gain strength allowed on the Advantage_system4.1 hardware. The intent of this schedule is to begin applying the h-gain field very quickly once the anneal starts using a high slope ramp up, and then to ramp down just before the anneal ends. However, the applied h_gain field is turned off both at the very start and very end of the anneal, with the field being turned off nearly 1 µs before the end of the anneal. The intention of beginning and ending the schedule in this manner is to allow the state transition measurement at the end of the anneal to be entirely based on the state of the system having been allowed to evolve a small amount before measurement without the applied h-gain field. The exact choice if timing here is based only on empirical results where the applied field was strong enough to get many states into the intended ground state, but not so strong as to overwhelm the anneal immediately into the intended ground state. Other choices of h_gain_schedule also have these properties and could be utilized in the future as well; for example, smaller pulses of h-gain fields could be used to induce smaller "pushes" towards an intended state. This choice of h-gain schedule satisfies another constraint of the Advantage_system4.1, which is that the maximum number of points we can use to define the $g(t)$ function is 20. The maximum slope present in the h_gain_schedule is also constrained, which is the reason for the jumps of 0.05 µs. Although not used in our methodology, the h_gain_schedule is also allowed to have negative values. When instantiated in the hardware, the user-programed points are linearly interpolated in between, and a continuous function over time is created, which is then implemented in the hardware.

The initial variable state is specified using the *reverse annealing* control feature of the D-Wave quantum annealer. Reverse annealing is a variant of quantum annealing, which begins and ends the anneal in classical states, where the beginning state is programed by the user, and over the duration of the anneal the system can be set to different anneal fractions s over time with the goal of improving upon the initial state the anneal began with [43,68,104–109]. Programming reverse annealing consists of specifying three different parameters. First, the boolean state `reinitialize_state` must be specified, which dictates whether the state is reinitialized after each read out or not. For all experiments we set `reinitialize_state` to True. Next the anneal schedule is chosen, which needs to begin and stop in the classical state (meaning the anneal fraction $s = 1$). The reverse annealing schedule is fixed to `[[0.0, 1.0], [20, 0.65], [80, 0.65], [100, 1.0]]` where the first coordinate is time in microseconds and the second coordinate is the anneal fraction s. The reverse annealing schedule was chosen to have a standard ramp up and ramp down that is symmetric, both with a duration of 20 µs. The anneal fraction to pause at was chosen empirically so as not to overwhelm the samples with either the initial state or the intended state—in other words, these parameters were chosen such that the response curves were not flat. A smaller anneal fraction during the pause (for example, 0.5 or 0.4) would make the state transitions overall more susceptible, and a larger anneal fraction (for example, 0.8) would make the state transitions less susceptible. Lastly, we need to specify the initial classical state for all active qubits. This is done using the `initial_state` parameter, which encodes the variable states as spins of either 1 or -1. As with the h_gain_schedule, the programed points that define the anneal schedule are linearly interpolated between in order to create a continuous anneal schedule over the anneal time which is implemented in the hardware.

Each device call uses exactly 1000 anneals. Every other parameter is set to default; for example, `auto_scale` is set to True. The `annealing_time` is always 100 µs. Both the `programming_thermalization` and `readout_thermalization` are set to 0 µs.

Combining reverse annealing to specify an arbitrary initial state and the *h-gain state encoding* to specify a final state results in the unified *state transition susceptibility mapping* technique. For simplicity and because the annealing process naturally tends towards ground states by design, we restrict the intended final states to be those of optimal solutions, or ground states, of the problem Ising models. Data which show the success proportion of how many final states were the intended ground state as a function of increasing the parameter h for the h-gain schedule will be referred to *h-gain response curves*. To denote this mapping procedure, we will use $A \rightarrow B$, where A is any classical initial state and B is any classical ground state of the problem Ising.

C. Metrics and algorithms

The primary quantity of interest in these experiments is the proportion of samples, out of all measured samples across the 1000 anneals and hundreds of embedded instances which we will denote as $n\_samples$, that are in the ground state that was encoded in the linear terms of the problem. Given we find that n_GS samples are in this specific ground state, we will define this proportion of ground-state samples:

$$P_{\text{GS}} = \frac{n\_GS}{n\_samples}. \quad (4)$$

Because each D-Wave backend call requests 1000 samples and the Ising is embedded multiple times on the hardware, the total number of samples for each device call is $n\_samples = 722\,000$ for the N_6 Ising, $n\_samples = 625\,000$ for the N_7 Ising, and $n\_samples = 525\,000$ for the N_8 Ising. This experimental setup allows for robust sample sizes to be collected and to get high-accuracy simulation results.

Having enumerated across all h strengths $\in [0, 3]$ in steps of 0.1 indexed by the variable j, we get a P_{GS} measure for each of those different h strengths. From these measures, we create a *susceptibility* metric defined in Eq. (5), which describes the amount of h-gain strength that was required to move the anneal from the initial state (encoded using reverse annealing) to the specified ground state (encoded using the h-gain state encoding method),

$$\chi = \frac{\sum_{j=0}^{30} P_{\text{GS}_j}}{30}. \tag{5}$$

The susceptibility metric captures across all measured h-gain strengths how successful this mechanism was at causing the system to end in the intended ground state. If $\chi = 1$ (e.g., high susceptibility), at every amount of applied h the system $A \rightarrow B$ was *very susceptible* to transitioning to the target ground state. If $\chi = 0$ (e.g., low susceptibility), there were no samples from the quantum annealer at any value of h that were measured in the intended ground state—indicating that the mapping system $A \rightarrow B$ was *not susceptible* to transitioning to the target ground state. In practice, no states will have exactly $\chi = 0$ or 1 due to the high measurement count and the noise present on the device. Note that this metric is similar to measuring magnetic susceptibility in other contexts of quantum annealing (see [1,100,110]), however it is slightly different in that it is a sum over several h-gain strengths, not a single pulse, and the system was in a very specific initial state due to reverse annealing.

One of the interesting trends that is observed in the data, which will be explored in detail in Sec. III, is a consistent lower overall susceptibility measure for some states that are very near the ground state in terms of hamming distance, but not necessarily close in terms of other relevant metrics such as the energy of the state. It turns out that these states that exhibit very high susceptibility towards the ground state are one bit flip away from the ground state, but the index of that bit flip corresponds to the highest degree node in the Ising graph. To determine whether this trend is consistent across other states (and across all three test Ising models), we define a metric δ on states to be maximized where the state is exactly one highest degree variable away from a ground state, and minimized for the state that is the complement of the ground state. This metric is based on defining the subset V of variables out of the variables in a given initial state i whose state is opposite that of the ground state we are pushing the system into. Thus if V contains one variable, then our state i is exactly one bit-flip away from the ground state, and if V contains the same number of variables as the Ising, then the given state i is exactly the complement of the ground state. Assume the procedure *G_deg* computes the degree of the variable v of the specific Ising graph G,

$$\delta = \frac{\sum_{v \in V} \text{G\_deg}(v)}{\text{length}(V)} \cdot \frac{1}{\text{length}(V)}. \tag{6}$$

Equation (6) is undefined when the initial state is the same as the ground state because in that case $V = \varnothing$; therefore, when this case occurs we set $\delta = M + 1$, where M is the largest degree in the Ising graph.

Two other metrics that will be utilized are as follows:

(i) The energy of the initial state evaluated on the given test Ising (either N_6, N_7, or N_8). We denote the energy metric as $E(i)$ for the initial state vector i.

(ii) The hamming distance between the initial state and the intended ground state as a proportion of the number of variables. The hamming distance proportion is denoted as $d(i, \text{GS})$ for the initial state vector i and the ground-state vector GS.

To help differentiate some of the different observed h-gain response curves, *unsupervised spectral clustering* is performed on the vectors of the h-gain response curves. Specifically, we cluster the vectors for each collection of h-gain response curves that are transitioning the annealer to a single ground state; this clustering is then repeated for each of the other ground states in the Ising. We cluster the data into four clusters across all experiments; this number of clusters is somewhat arbitrary and a similar number of clusters could be utilized, however four gives a reasonable balance between having reasonably distinct behaviors in the clusters while also being able to visually present all of the clusters in a reasonable amount of space. The spectral clustering implementation used is from the python library *scikit-learn* [111–117].

A natural question that arises in the state transition data is what intermediate states does the anneal pass through at different slices of h (i.e., the strength of the amplification of the ground state). One way to represent this process is to simply construct a graph that consists of the classical states represented as nodes and edges representing when moving from one h value to another changed the dominant classical state in the readout of the samples. For a single mapping procedure from one classical state to a ground state, this graph would simply be a path; the node representing the starting state is at one end, and the node representing the largest classical state found among all anneals at the readout when $h = 3$ (which we would expect to typically be the intended ground state). Then if there were any intermediate states that the anneal found across the increasing h strengths, we could connect these together in a linear line thus forming a simple linear nearest-neighbor (LNN) path. If there are no intermediate states (for example, if the samples immediately were pushed into the ground state), then the path would consist entirely of the two nodes and a single edge connecting them. Taking the union of each of these paths across all state mappings of initial state to ground state can then form a coherent state transition network for that problem Ising. This representation is a simplification of the data and the state transition process because it only forms edges for the dominant classical state found at each h step. However, this representation does give a notion of *distance* between the starting states and the ground states in the form of how many other states the anneal transitions to before reaching the ground state. For drawing these graphs, the layout used is the *spring layout* in the python Networkx [88] library, which in part uses the Fruchterman-Reingold force directed algorithm [118].

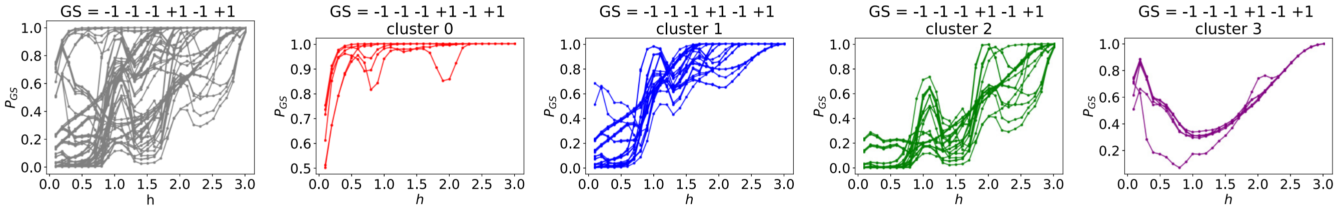

FIG. 3. The left-hand gray-colored plot shows the distribution of P_{GS} as h increases for transitioning all 2^6 input states into a single ground state (the exact ground state is shown in the title of each of the subfigures). The four rightmost plots split up these data into four distinct clusters using unsupervised spectral clustering of the vectors of P_{GS} values across the increasing h strengths. Each cluster of vectors is colored uniquely, and the coloring arbitrary and randomly chosen.

III. RESULTS

In this section, we present state transition mapping results for each of the three test Ising models. Section III A details results for the N_6 Ising, Sec. III B details results for the N_7 Ising, and Sec. III C shows results for the N_8 Ising. Section III D details the state transition network representation of the data. Section III E further investigates ground-state to ground-state transitions in each of the three test Ising models. Section III F analyzes what the h-gain susceptibility metric shows with regard to fair sampling—specifically how similarly the h-gain response curves and susceptibility quantities behave across the multiple ground states for each of the test Ising models. Lastly, Sec. III G examines the ground-state proportion sampling rate of the three test Ising models when only reverse annealing is applied in order to determine if there are similarities to the h-gain response curves.

A. N_6 Ising h-gain response curves

Figures 3 and 4 show the clustering results for two of the four ground states of the N_6 Ising. An interesting characteristic of the results shown in Figs. 3 and 4 is the similarity between them even though they are showing the h-gain response curve for two different ground states, and these two ground states are not complements of each other. This suggests that there is quite a bit of symmetry even in this problem Ising. While the h strength parameter is consistently increasing on the x-axis of both Figs. 3 and 4, we see that the h-gain response curves are *not* all monotonically increasing as a function of h. This means that this incremental increase of h is transitioning the annealing process into other intermediate states, including in particular other ground states, which would therefore necessarily decrease the success probability. The unsupervised clustering of the h-gain response curves helps to differentiate which response curves have a nonmonotonic response and which ones do not; for example, the cluster of red curves in Fig. 3 and the cluster of purple curves in Fig. 4 have identified a subset of states that required a comparably smaller amount of applied h strength in order to transition to the ground state. This state transition process will be investigated in more detail for ground-state to ground-state transitions in Sec. III E and in the form of a state transition network in Sec. III D. The h-gain response curves for the other two ground states are not shown here for brevity.

Figure 5 shows the susceptibility metric across all 2^6 initial states of the N_6 Ising when forcing the anneal into the four distinct ground states. An immediate observation that can be made on these data is that for each ground state, its complement is always the minimum susceptibility across all possible states.

Figure 6 shows scatterplots of the three metrics (hamming distance, energy, and δ) outlined in Sec. II C versus χ for each of the initial states. For each of these three metrics there are a couple of clear observations to be made. First, there is a consistent positive correlation between susceptibility and hamming distance proportion, where a higher hamming distance proportion leads to lower susceptibility. Second, there is seemingly very little trend between energy and susceptibility; we can see a clear stratification of states with a similar susceptibility being distributed across the entire energy spectrum of the Ising. Third, there does appear to be some correlation between δ and χ, where a larger δ corresponds to higher susceptibility.

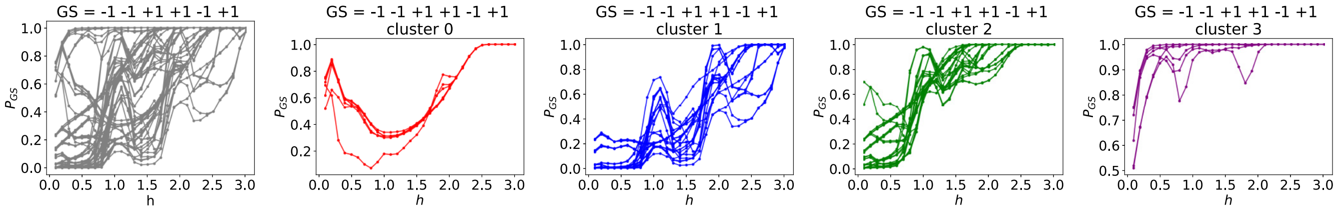

FIG. 4. The left-hand gray-colored plot shows the distribution of P_{GS} as h increases for transitioning all 2^6 input states into the single ground state (the exact ground state is shown in the title of each of the subfigures). The four rightmost plots split up these data into four distinct clusters using unsupervised spectral clustering of the vectors of P_{GS} values across the increasing h strengths. Note that this plot overall is very similar to Fig. 3, but is showing data for a different ground-state encoding (this ground state it turns out is hamming distance 1 away from the ground state in Fig. 3) and the ordering of the clusters is different.

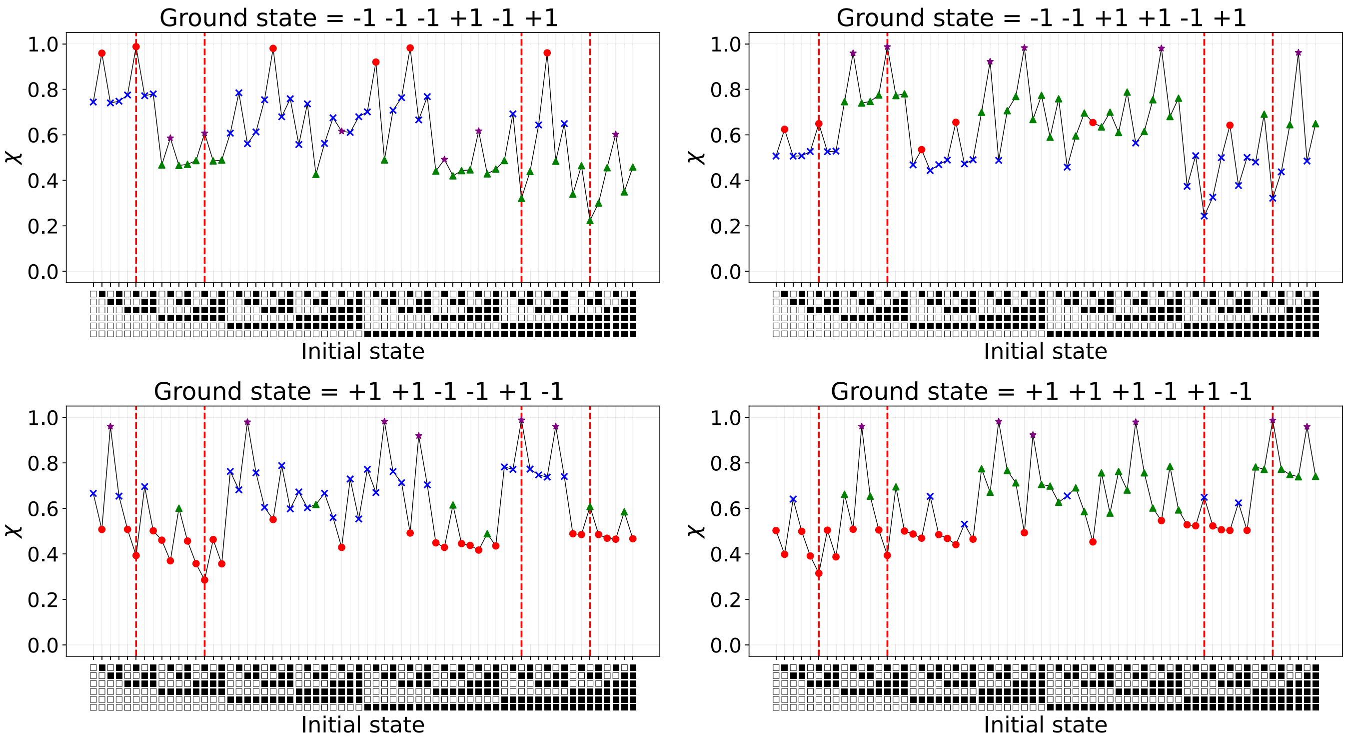

FIG. 5. N_6 Ising susceptibility across all 2^6 initial states when applying the h-gain schedule to force the system into each of the four ground states. The x-axis encodes these initial states as vectors of vertical blocks, where ■ denotes a variable state of $+1$ and □ denotes a variable state of -1. The initial state vectors are read from bottom to top, where the bottom is the first index which corresponds to variable 0 in the problem Ising. All initial states which are also other ground states are marked with dashed red vertical lines. For each subfigure, the reflexive ground-state mapping (i.e., where the initial state and the intended state are the same ground state) case can be found visually as the state marked with a red vertical dashed line, which has the maximum susceptibility measure among all of the initial states.

Figures 6 and 5 use the same coloring schemes from the spectral clustering done on the h-gain response curves, however the actual colors (i.e., index of the cluster) used are arbitrary and randomly assigned by the clustering algorithm. However, all of the figures follow consistent coloring schemes for each of the four different ground states. Note that because two of the h-gain response curves were omitted, the coloring of the other two datasets is not shown in Figs. 3 and 4. For a clear example, the clustering coloring used in Fig. 3 is the same coloring used in Fig. 5, top left, which is also the same coloring used in the left-hand column of Fig. 6; all of these plots are in some way representing and analyzing the same dataset where the *h-gain state encoding* was applied to a single one of the four ground states.

Examining the results from the h-gain response curve clustering (Figs. 3 and 4) in conjunction with Figs. 5 and 6, we can observe several interesting trends. First, we can clearly see the motivation for developing the δ metric in Sec. II C. Specifically, in Fig. 5 we see that when the initial state we encode using reverse annealing is also the ground state that is specified using *h-gain state encoding*, the susceptibility metric is at a minimum (i.e., it is nearly 0). This is to be expected, however we also see that there are several other states that have a relatively large susceptibility. However, these states are not ground states (ground states are marked in Fig. 5 using dashed red vertical lines). If we examine where these states occur in the block of subplots in Fig. 6, which can be done using the fixed clustered coloring scheme and the ground state labels on the titles, we see that there is apparently no correlation with respect to the energy of these states. There is some correlation with respect to the hamming distance proportion, namely that all of the hamming distances are $\leqslant \frac{2}{3}$. The interesting property of these high susceptibility states is that they are very close to the ground state in terms of hamming distance (i.e., bit flips), but only for variables that are high degree in the graph of the Ising problem; this is the observation that led to the creation of the δ metric.

As a specific example, we can examine Fig. 5, upper left-hand subplot. The ground state in this plot has variable assignments $[-1, -1, -1, +1, -1, +1]$, where the index denotes the variable in the original Ising problem. There are a total of six initial states that are colored red in this plot, meaning that their h-gain response curves all behaved similarly, and indeed we see these six states have the highest susceptibility metrics among all 2^6 states. The two states that have the largest susceptibility metric besides the ground state are $[-1, +1, -1, +1, -1, +1]$ and $[+1, -1, -1, +1, -1, +1]$. Now if we examine Fig. 1 for N_6 (left-hand graph), we see that variables 0 and 1 both have a degree of 5, which is the largest degree in the graph. Examining these two other states which had maximum susceptibility shows that they are both exactly one bit-flip away from the ground state—specifically if we flip $[-1, +1, -1, +1, -1, +1]$ at index 1 from a $+1$ to a -1, we get the ground state. And if we flip $[+1, -1, -1, +1, -1, +1]$ at index 0 from a $+1$ to a -1, we also arrive at the ground state. If we evaluate these two states using Eq. (6), we get a

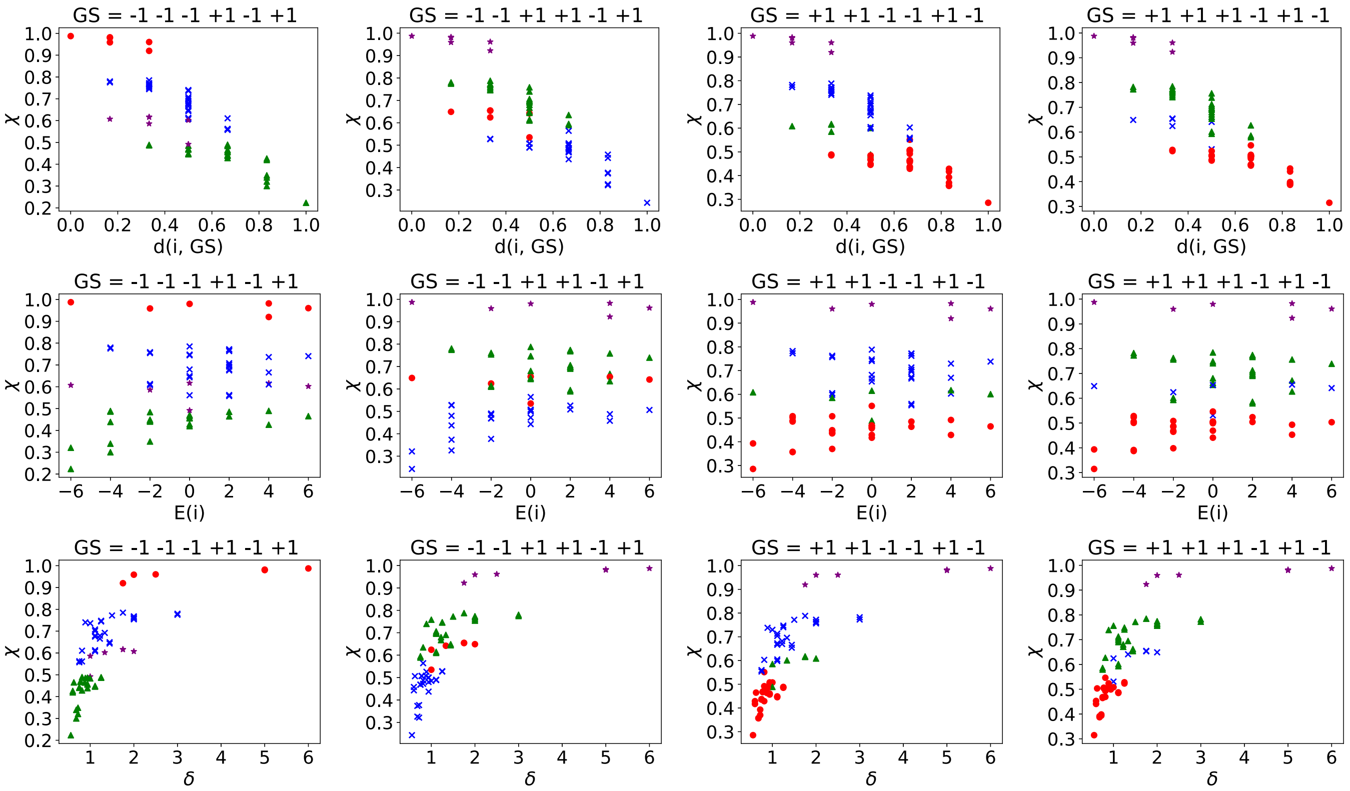

FIG. 6. Summary metric plots for the N_6 Ising. The 4 columns correspond to each of the 4 ground states; the titles of each subplot are the exact optimal solution vectors. The three rows correspond to three different initial state metrics on the x-axis; the y-axis of each subplot is the susceptibility metric χ. The first row has the x-axis, which is the hamming distance between the ground state and the specific initial state i. The second row has the x-axis showing the energy of the initial state i evaluated on the N_6 Ising. The third row has the x-axis showing the δ metric for each initial state.

value of 5 because these states are exactly one degree 5 variable away from the ground state. The points corresponding to these two states appear in Fig. 6 in the bottom left-hand corner plot where both χ and δ are overlapping, causing them to appear as a single point. High degree variables in the problem Ising being easier to induce a bit flip in comparison to most other states is consistent with how the physical device implements these problems, namely that these high degree variables have more constraints acting on them compared to the rest of the variables, which then requires smaller h-gain amplification of the linear terms encoding the ground state to change the state of the variable compared to other initial states.

B. N_7 Ising h-gain response curves

Figure 7 shows the h-gain response curves for all initial states along with the four groups of clustered response curves for one of the two ground states for the N_7 Ising results. As with the N_6 h-gain response curves, Fig. 7 shows non-monotonic increases of P_{GS} as a function of increasing h for most initial states, again suggesting that the process is getting trapped in other intermediate states besides the intended ground state. For brevity, the response curves for the other ground state is omitted. Figure 8 shows the susceptibility metric across all 2^7 initial states of the N_7 Ising when applying the *h-gain state encoding* for each of the two ground states. Figure 9 shows scatterplots of the three metrics (hamming distance, energy, and δ) outlined in Sec. II C versus χ for all of the initial states. Compared to the N_6 Ising results in Sec. III A, these results look similar and have similar patterns overall. For example, the δ metric still reasonably applies to high susceptibility initial states. The h-gain response curve plot (Fig. 7) is noticeably different from the h-gain response curves of the N_6 Ising in Figs. 3 and 4. In Fig. 8, because this Ising has exactly two ground states which are complementary, we can observe a clear symmetry in the data—these two plots are mirrors of each other if reflected about the midline of the initial state vectors on the x-axis. This is especially clear because of the two ground states, but a similar symmetry between the pairs of ground states in the N_6 Ising can also be seen in Fig. 5.

Overall, the results for the N_7 Ising are consistent with the same trends and observations made on the N_6 Ising, despite the additional variable and decreased number of ground states.

C. N_8 Ising h-gain response curves

Figure 10 shows the h-gain response curves for all initial states along with the four groups of clustered response curves for one of the two ground states for the N_8 Ising results. Figure 11 shows the susceptibility metric across all 2^8 initial states of the N_8 Ising when applying the *h-gain state encoding* for each of the two ground states. Figure 12 shows scatterplots of the three metrics (hamming distance, energy,

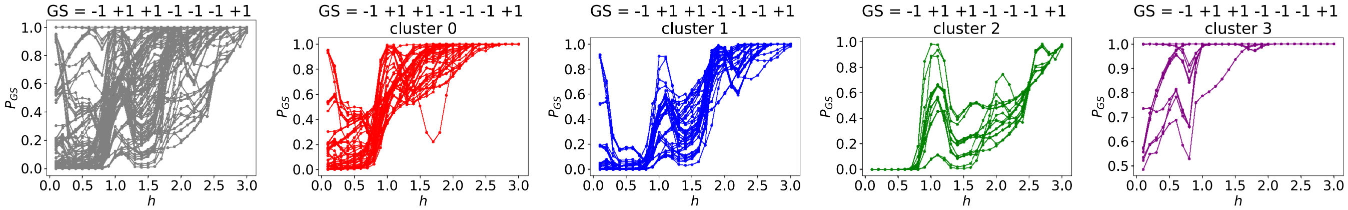

FIG. 7. The left-hand gray-colored plot shows the distribution of P_{GS} as h increases for transitioning all 2^7 input states into a single ground state for the N_7 Ising (the exact ground state is shown in the title of each of the subfigures). The four rightmost plots split up these data into four distinct clusters using unsupervised spectral clustering of the vectors of P_{GS} values across the increases h strengths.

and δ) outlined in Sec. II C versus χ for all of the initial states.

The top row of Fig. 12 has noticeably different characteristics compared to the other hamming distance proportion plots from the N_6 and N_7 Ising (Fig. 6, top row and Fig. 9, top row). The plots for the N_6 and N_7 Ising have a roughly linear relationships between the hamming distance proportion and susceptibility. However, in the corresponding plot for the N_8 Ising (Fig. 12, top row) we see a slightly different trend occurring; the points appear to have a concave shape facing towards the bottom left-hand corner of the plot (and a convex shape facing towards the bottom right-hand corner of the plot). This appears to be a result of most of the h-gain response curves having a lower success rate of managing to get the anneal into the intended ground state compared to the smaller N_6 and N_7 Ising models. This could also be a result of the increased number of ground states for this Ising, which could be causing anneals to be trapped in nonintended ground states (this is investigated further in Sec. III E).

As with the other two test Ising models, there were not any nonsymmetric results across the different ground states—either all of the ground states behaved roughly the same for a given metric, or sets of ground states displayed clear symmetries.

D. State transition networks

Figure 13 shows graphical representations of the state transition networks for each of the three test Ising models. These state transition networks contain several notable characteristics. First, the nodes that represent the ground states are the highest degree nodes in the graphs, which is expected since they are the intended end point of the state transitions. Second, it is not the case that all non-ground-state nodes have an edge directly connecting them to the ground-state nodes. Such a direct edge connection would mean that the susceptibility of moving the anneal into the intended ground state did not pass through other intermediate states. Instead, we see that for some states the path to the ground states could contain several other nodes. Third, there are some states that are consistent intermediate states for clusters of nodes; in the leftmost graph these nodes are the eight orange nodes which are persistent intermediate states for small groups of classical states. Fourth, there are clear symmetries in these graphs with respect to the local communities of nodes that are connected similarly, or identically, in other parts of the graph.

The N_8 state transition graph in Fig. 13 has fewer discernible trends compared to the state transition graphs for the N_6 and N_7 Ising models. This is largely due to the increase in the number of nodes and edges present in the graph, which is due both to the increase in the number of classical states (256 in total) as well as the increase in the number of ground states (8). What is clear from the state transition graph in Fig. 13 is that there are many intermediate states during the transition from one state to a ground state.

E. Ground-state to ground-state transitions

Here we specifically highlight some of the state transitions that are of particular interest—those being ground-state to ground-state transitions and what intermediate states are found during the transition from one ground state to another.

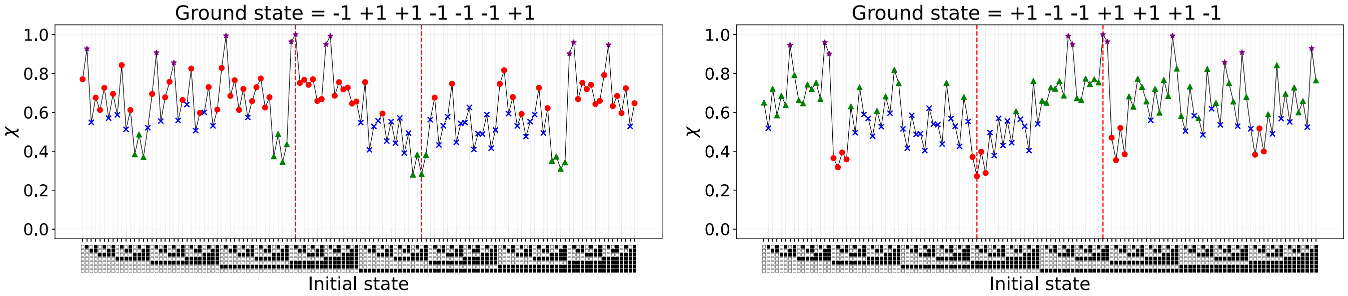

FIG. 8. N_7 Ising susceptibility across all 2^7 initial states when applying the h-gain schedule to transition the system into each of the two ground states. The x-axis encodes these initial states as vectors of vertical blocks where ■ denotes a variable state of 1 and □ denotes a variable state of -1. The initial state vectors are read from bottom to top, where the bottom is the first index which corresponds to variable 0 in the problem Ising. The initial states which are also other ground states are marked with dashed red vertical lines. For each subfigure, the reflexive ground-state mapping (i.e., where the initial state and the intended state are the same ground state) case can be found visually as the state marked with a red dashed vertical line, which has the maximum susceptibility measure among all of the initial states.

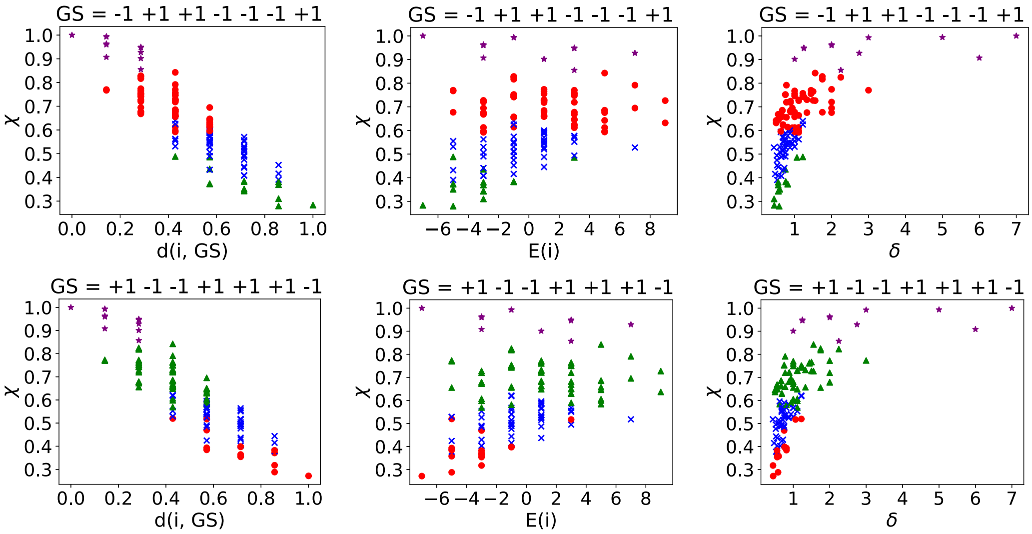

FIG. 9. Summary metric plots for the N_7 Ising. The two rows correspond to each of the two ground states; the titles of each subplot are the optimal variable assignment vectors. The three columns correspond to three different initial state metrics on the x-axis; the y-axis of each subplot is the susceptibility metric χ. The first column has the x-axis that is hamming distance between the ground state and the specific initial state i. The second column has the x-axis showing the energy of the initial state i evaluated on the N_7 Ising. The third column has the x-axis showing the δ metric for each initial state. The node colorings for the top row of subfigures share the same node coloring as Fig. 8, left, and the node colorings for the bottom row of subfigures share the same node coloring as Fig. 8, right.

These response curves provide some intuition as to how quantum annealing works, at least in the reverse annealing mode. Specifically, moving from one ground state to another ground state does not require zero h-gain strength. Indeed, as seen in Sec. III A, the complementary ground states in the N_6 Ising had *maximal* susceptibility when switching from the initial ground state to its complement.

Figure 14 shows a detailed analysis of a subset of ground-state to ground-state transition curves for the N_6 Ising in terms of the proportion of samples that were each of the four ground states as well as higher-energy states. The h-gain response curves (Figs. 3, 4, 7, and 10) and the state transition networks in Fig. 13 have all shown that during this state transition induced by the increasing h strength, the samples are not immediately flipped from the initial state into the intended ground state. Instead, the variable states are each flipped at different rates in response to the increase in applied h; the δ metric is a clear example where a single variable can be more susceptible to flipping its state compared to other variables due to properties of the problem Ising. Figure 14 shows for each increase of h what other states the samples end up in, which clearly shows that transitioning from one state to another flips the variable states at different rates causing the anneal to end up in other intermediate states.

Because of the h-gain initial state encoding scheme [43], the optimal solution of the Ising (the problem Ising is a union of the problem Ising quadratic terms and the complement of the intended ground state) is simply the intended ground state. As we increase h, the objective function evaluation of that optimal solution decreases. Therefore, it is a notable observation that in Figs. 14 and 15 we do not see a monotonic increase in the proportion of the intended ground state—indeed it seems to fluctuate, and at roughly $h = 1.5$ there a local minimum across all of the plots (at least for the nonreflexive ground-state mappings). This shows, as observed in the other data analysis, especially in Sec. III D, that there are paths being traversed in the search space of this reverse annealing procedure which are not always in an optimal solution.

F. Fair sampling analysis

Given that quantum annealing in the transverse field Ising model is known not to sample ground states fairly, it is natural to ask whether these state mapping enumeration results show

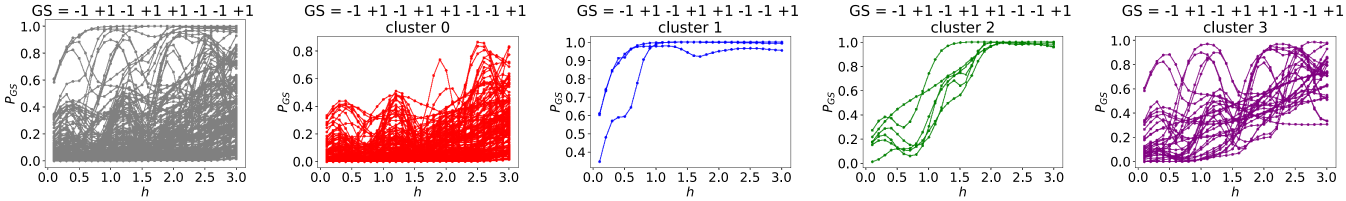

FIG. 10. The left-hand gray-colored plot shows the distribution of $P_{\rm GS}$ as h increases for transitioning all 2^8 input states into a single ground state for the N_8 Ising (the exact ground state is shown in the title of each of the subfigures). The four right-hand plots split up these data into four distinct clusters using unsupervised spectral clustering of the vectors of $P_{\rm GS}$ values across the increases h strengths.

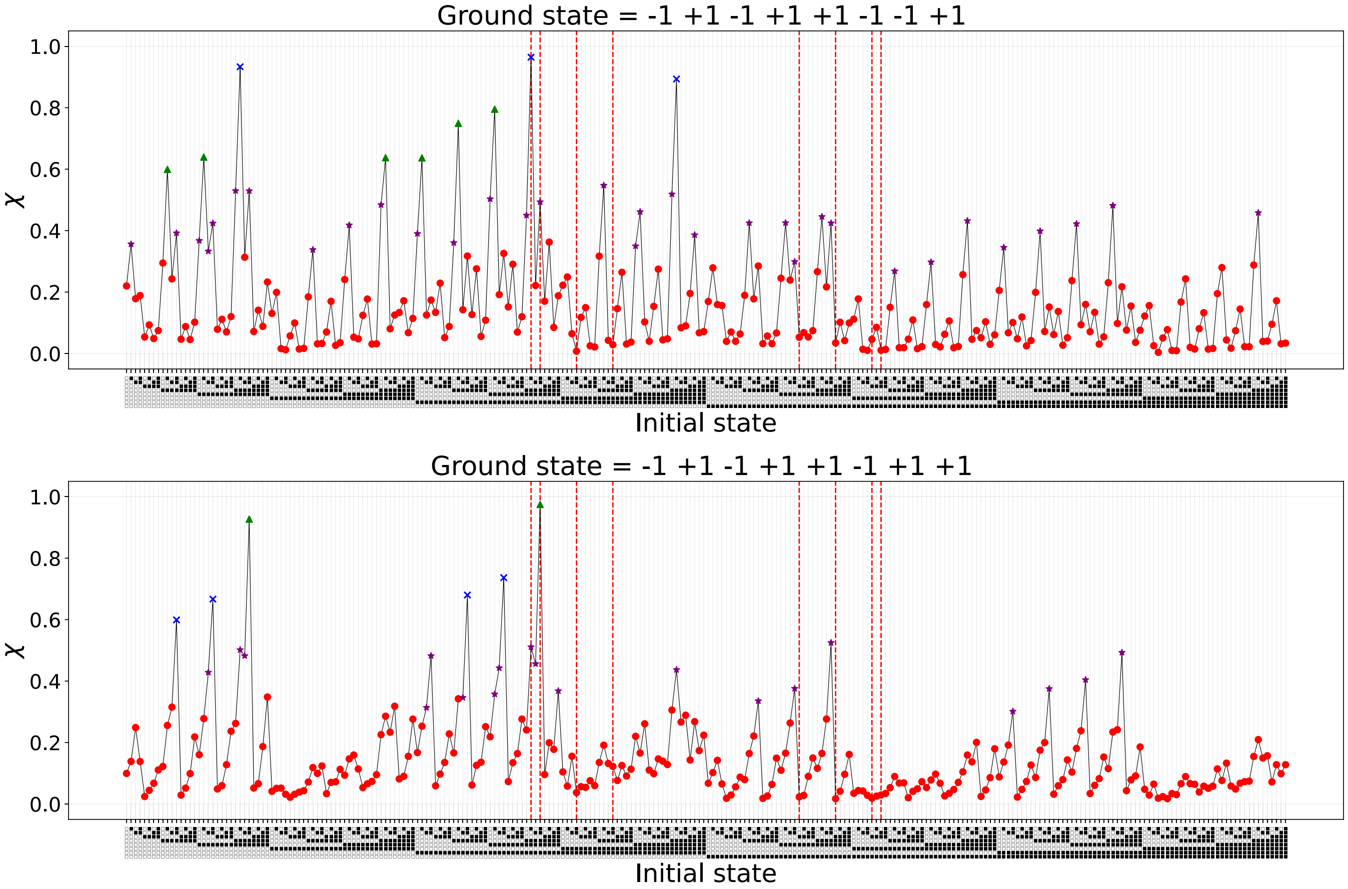

FIG. 11. N_8 Ising susceptibility across all 2^8 initial states when applying the h-gain schedule to push the system into two out of the eight ground states where the two subfigures represents one ground-state transition. The other six ground-state plots are shown in Fig. 22 in Appendix. The x-axis encodes the initial states as vectors of vertical blocks where ■ denotes a variable state of $+1$ and ☐ denotes a variable state of -1. The initial state vectors are read from bottom to top, where the bottom is the first index which corresponds to variable 0 in the problem Ising. The initial states which are also other ground states are marked with dashed red vertical lines. For each subfigure, the reflexive ground-state mapping (i.e., where the initial state and the intended state are the same ground state) case can be found visually as the state marked with a red vertical line, which has the maximum χ measure among all of the initial states.

a bias for a particular ground state or set of ground states. In particular, for a set of state transition mappings from all initial states to a ground state, the question is if the average susceptibility across all of those initial states is very different when comparing the different ground-state mappings. Figure 16 shows this comparison across the three test Ising models. Interestingly, the average susceptibility distributions for the N_6 and N_8 Ising are not uniform across the ground states, although in the N_7 Ising case the two ground states appear to have very close average susceptibility.

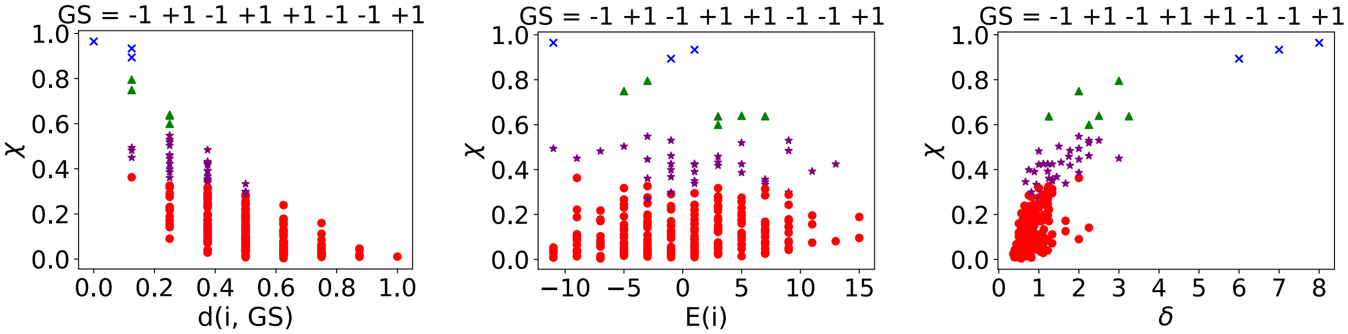

FIG. 12. Summary metric plots for the N_8 Ising. These three plots show χ on the y-axis, plotted against hamming distance between the ground state and the specific initial state i (left), the energy of the initial state i evaluated on the N_8 Ising (middle), and the δ metric for each initial state (right). These data are only for the h-gain mapping to the first ground state—the mappings to the other seven ground states of the N_8 Ising are displayed in Fig. 23 in Appendix.

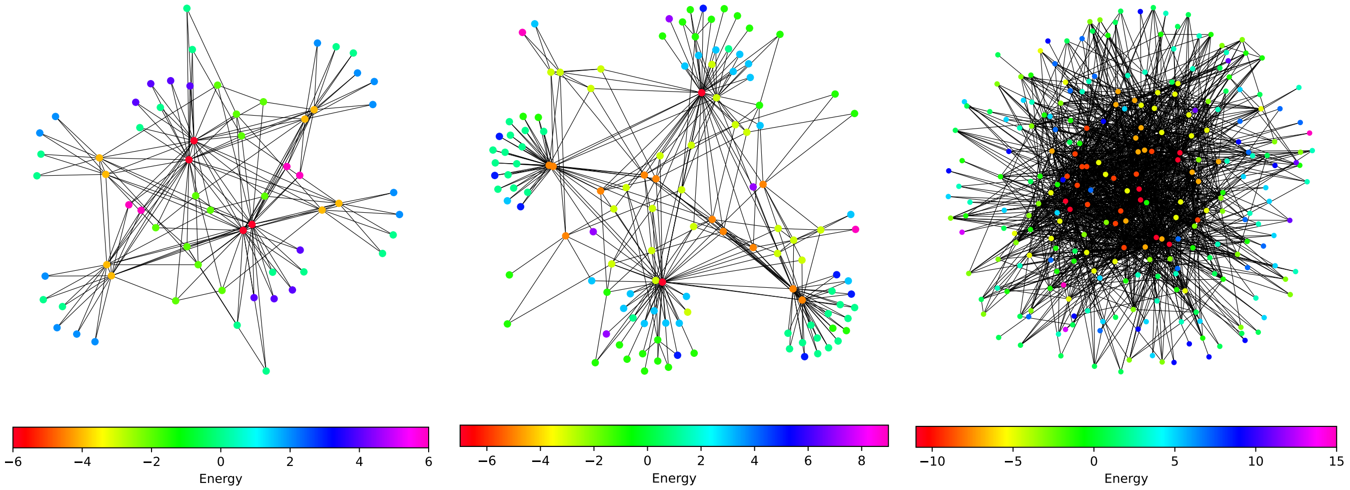

FIG. 13. State transition networks for the N_6 Ising (left), N_7 (middle), and N_8 (right) when aggregating the *h*-gain response curves across all mappings for each ground state. Each node represents one classical state; the N_6 graph has 64 nodes, the N_7 graph has 128 nodes, and the N_8 graph has 256 nodes. The nodes are colored corresponding to the energy (i.e., objective value) of that state evaluated on the Ising, the heatmaps for which are shown below each graph. The red node represents the ground-state solutions of the problem Ising, and the purple nodes represent the highest energy states of the problem Ising.

Another interesting question could be if the nonuniform distribution in Fig. 16 is also present when applying forward annealing to the test Ising models. To this end, a small set of experiments with forward annealing was performed on the three test Ising models. The device parameters were 10 000 anneals and 100 μs of annealing time for consistency with the state mapping experiments, readout_thermalization of 0 μs, programming_thermalization of 0 μs. The same device, D-Wave Advantage_system4.1, was used for these experiments. The same parallel disjoint embeddings outlined in Sec. II A were utilized. Figure 17 shows the ground-state proportion (GSP) from these forward annealing experiments across the three test Ising models. The forward annealing GSP results clearly show a consistent bias for some ground states, which is in agreement with previous D-Wave quantum annealing fair sampling experiments [66,67,69], particularly for the N_8 Ising, although the differences are less significant especially for the N_7 Ising. Note that the sum of the ground-state proportions in each plot is always equal to 1, as opposed to Fig. 16 where the *y*-axis is simply average χ. Nevertheless, these plots can be compared to see if there are consistencies, for example, if the states that are broadly more difficult to transition into during the state mapping procedure are also sampled with a lower success proportion during forward annealing. Such a trend does not appear in the data. Even though both the distributions of forward annealing ground-state proportions and the average susceptibility are nonuniform, there does not appear to be consistency on the distributions. Susceptibility measurements using *h-gain state encoding* for forward annealing might provide more insight into the behavior of unfair sampling in quantum annealers.

G. Reverse annealing only

A natural question here is how reverse annealing (RA) by itself samples these optimization problems. And along with how RA does this for each of the initial states, another relevant question is how the success probability of sampling the optimal solution in RA correlates with χ. It would make sense

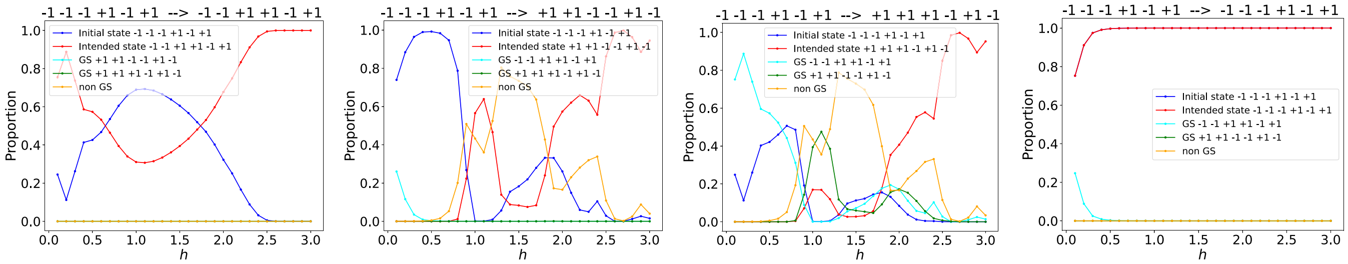

FIG. 14. A more detailed analysis of ground-state to ground-state *h*-gain response curves in the N_6 Ising. Here the initial state is the same for each of the three plots, and the proportion of the samples at each *h* increment which were in this initial state is colored blue. The titles of each subfigure show the direction of the state transition. The red lines in the three plots denote the proportion of samples that were the intended ground state. The cyan and green lines denote the proportion of samples which were in the remaining two ground states. The orange lines denote all remaining samples which were not in either of the four ground states. Note that, as mentioned in Sec. II A, these problems have complementary ground-state solutions; the middle-right-hand subplot shows the state transition from a ground state to its complement. The reflexive self-mapping of the ground state to itself is shown in the right-hand plot, which shows little state change as a function of *h*.

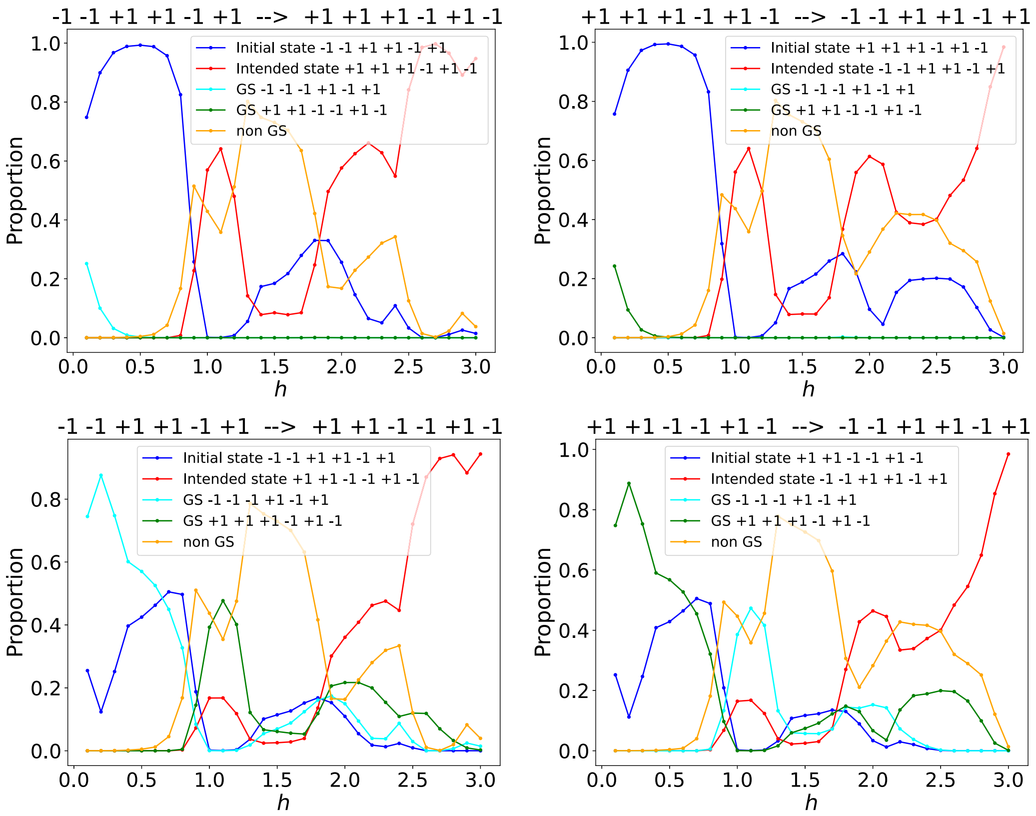

FIG. 15. Two examples of the symmetry of the ground-state to ground-state h-gain response curves in the N_6 Ising. The two rows are showing two different symmetric state mappings (e.g., $A \rightarrow B$ and then $B \rightarrow A$). The noticeable property of these plots is that the response curves have a clear symmetry, where when the two ground states are swapped a nearly identical response curve for all four ground states emerges (the difference is simply which place each ground state takes in the plots). Notice as well that the states in the bottom row are complementary ground states, whereas the ground states in the top row are not complementary ground states.

for these two metrics to correlate such that a higher success probability for an initial state reaching some ground state in RA corresponds to higher susceptibility of mapping that initial state to that ground state with RA and h-gain.

Because of the dynamics observed in the previous section (in particular, Sec. III D), we know that in this RA setup states will transition into intermediate states as h increases while the anneal is minimizing the state towards the

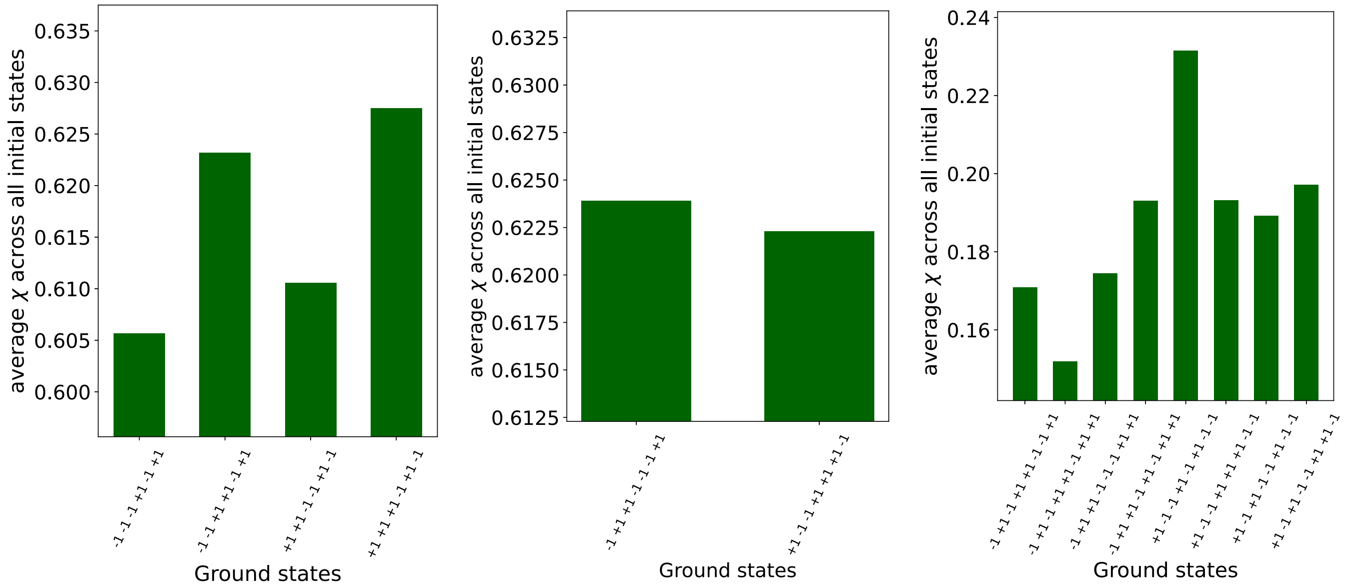

FIG. 16. Distribution of the average susceptibility (y-axis) across all initial states when transitioning the annealer into different ground states (x-axis) for the N_6 (left), N_7 (middle), and N_8 (right) Ising models.

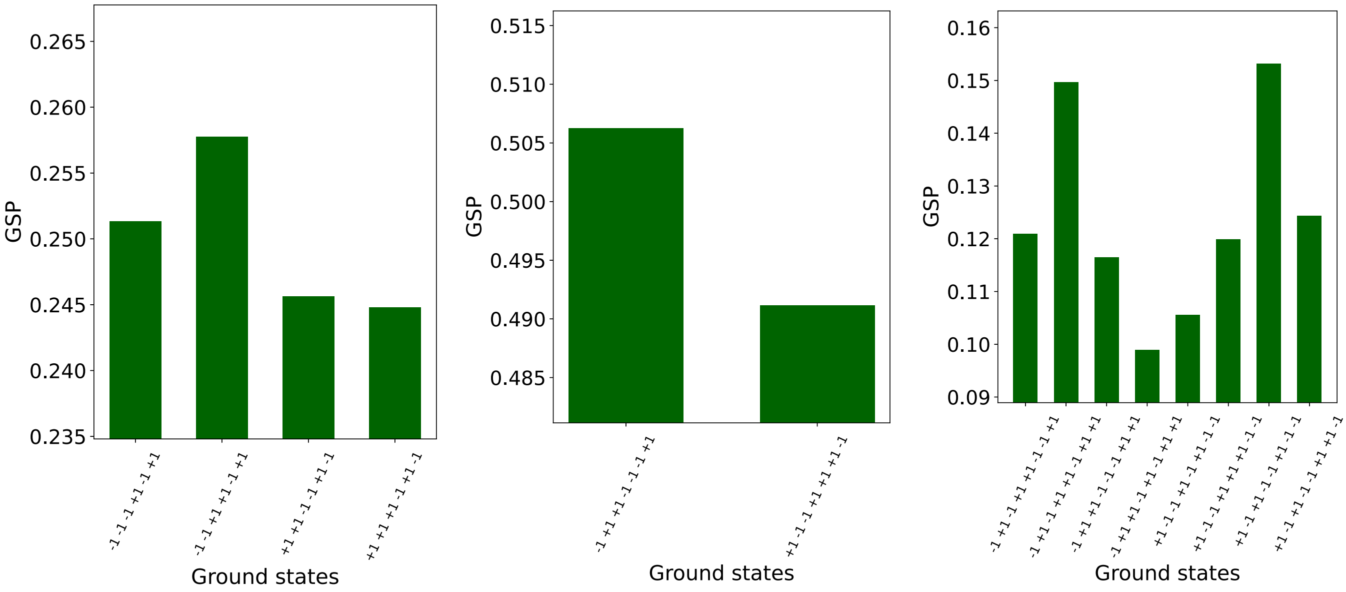

FIG. 17. Ground-state (x-axis) vs ground-state proportion distribution (y-axis) for the N_6 (left), N_7 (middle), and N_8 (right) Ising models having been executed on using forward annealing with no schedule modification and an annealing time of 100 μs.

programed optimal solution. Therefore, these intermediate states may cause the χ metric to not correspond directly to the plain RA success probability. On the other hand, it would be expected that there is a correlation between the RA ground-state probability and χ, which would confirm that in RA (with some initial state) some states are much easier to transition into than others.

Figures 18–20 show the RA ground-state proportions across all initial classical states. Notice that for these data, no unsupervised clustering of the data was applied, and therefore all of the nodes are colored the same. The dynamics of these figures are different from the RA and h-gain state transition mapping procedure plots, namely Figs. 5, 8, and 11. However, there are some similarities. First, the different ground-state plots are still symmetric for complementary ground states. Second, the reflexive ground-state mappings have the highest success rate, whereas the complementary ground states have the lowest ground-state success probability.

Figure 21 shows the correlation between χ and RA P_{GS} for the three test Ising models. Here the data are not being separated based on the ground state to which the mapping was applied, and instead all of the results are aggregated together into a single dataset. The Pearson correlation coefficient, computed with scipy [119], shows a linear relationship between RA P_{GS} and χ, as expected.

IV. DISCUSSION AND CONCLUSION

In this article, we present a method for quantifying the hardness, analogous to the susceptibility, of transitioning a quantum annealing system from one classical start at the beginning of the anneal to a classical ground state of a problem Ising at the end of the anneal. A full enumeration across all initial states was executed on three small test Ising models embedded in parallel on the D-Wave `Advantage_system4.1` quantum annealing processor. Importantly, this state transition susceptibility does not necessarily generally apply to forward annealing because the methodology specifically uses reverse annealing to encode a classical initial state. However, this state susceptibility enumeration does allow for an examination of interesting dynamics in the quantum annealer. In particular, it allows us to develop a notion of *distance*, or hardness, for moving between two classical states in a quantum annealer. This proposed state mapping procedure may be able to help in examining quantum annealing dynamics, when sampling ground states, by viewing the internal (not directly measurable) QA dynamics as a linear combination of the full 2^n initial state mapping. Section III F showed that the 2^n state mappings do not provide a mechanism to explain fair sampling QA dynamics assuming a uniform linear combination of the state mappings, but perhaps more advanced models would be able to better analyze QA behavior using these state mappings.

The set of data across the N_6, N_7, and N_8 Ising models are notable because there is a clear finding that, at least for reverse annealing with an anneal fraction of $s = 0.65$, low-energy states are not necessarily easily accessible from all input states. For the purposes of improving reverse annealing, selecting states that are near to the ground state with respect to certain metrics, such as hamming distance or the δ measure, could be beneficial, as opposed to selecting states that are simply low in energy, which could actually be a large distance away from the ground state in terms of the quantum annealing process. The observation that the success probability of reverse annealing is largely determined by the hamming distance of the initial state compared to the ground state has been quantified since the inception of reverse annealing [107]. This study is therefore consistent with previous reverse annealing findings, but it also presents a more detailed mapping of the state transition process.

Utilizing this mapping technique across input states and having some states substantially more accessible as defined

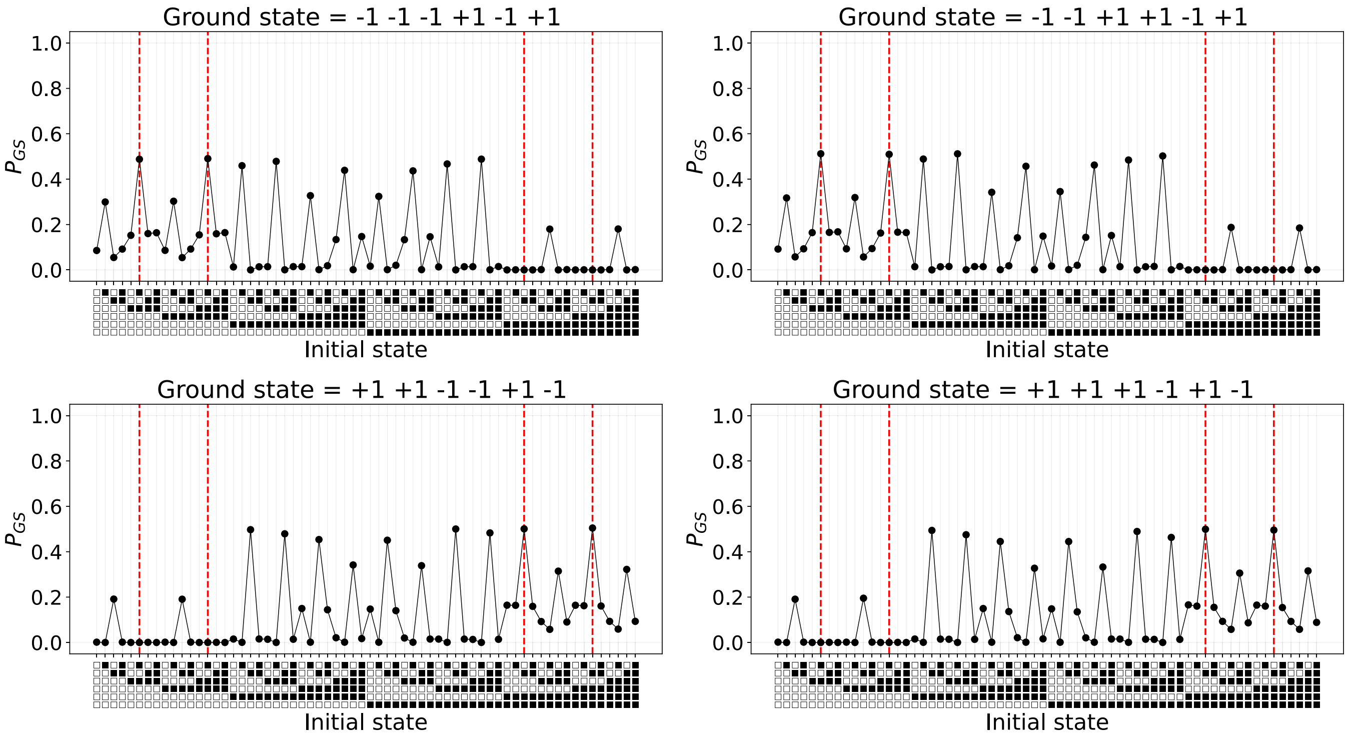

FIG. 18. Ground-state success probability for reverse annealing only, applied on the N_6 Ising. The x-axis encodes the RA initial states as vectors of vertical blocks, where ■ denotes a variable state of $+1$ and □ denotes a variable state of -1. The initial state vectors are read from bottom to top, where the bottom is the first index which corresponds to variable 0 in the problem Ising. The initial states which are also other ground states are marked with dashed red vertical lines. There are clearly some initial states that cause the reverse annealing P_{GS} to be much higher compared to other initial states.

by the δ metric could allow for improved design of test instances with planted solutions for reverse annealing, particularly because one could construct problems with initial states that are far away from the optimal solution by objective function evaluation but are easy for the annealer to transition to the optimal solution. Typically problems with known planted solutions [120–131] are intended to serve as a benchmark for how accurate quantum annealing and other heuristic computation tools are for problem sizes for which the optimal solution is difficult to compute exactly in reasonable time. However, specifically constructing planted solutions and specific initial states to begin the optimization is not a tool that has been developed for reverse annealing. Applying the full classical state enumeration that is utilized in this article is costly because it scales exponentially as 2^n states for n variables. Therefore, for practical reasons this type of state mapping will need to be restricted to small problem instances.

Examining how initial state choices impact the optimization process is not only relevant for quantum annealing, but it is also a relevant question in warm-start QAOA [132,133]. Because the Quantum Alternating Operator Ansatz (QAOA) algorithm [134] is effectively a Trotterization of quantum annealing, understanding the dynamics of variable state changes in quantum annealing could inform QAOA algorithm development. For example, it has been observed that in specific cases warm start QAOA for nonoptimal low-energy initial solutions gets stuck in local minima [132].

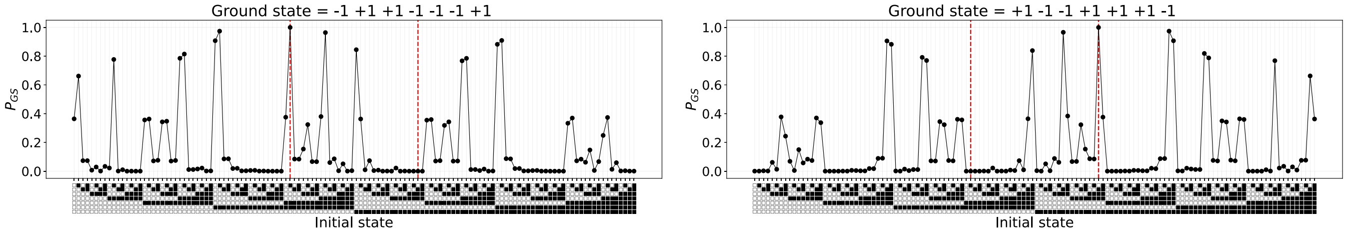

FIG. 19. Ground-state success probability for reverse annealing only, applied on the N_7 Ising. The x-axis encodes the RA initial states as vectors of vertical blocks, where ■ denotes a variable state of $+1$ and □ denotes a variable state of -1. The initial state vectors are read from bottom to top, where the bottom is the first index which corresponds to variable 0 in the problem Ising. The initial states which are also other ground states are marked with dashed red vertical lines. Because there are exactly two ground states, we can visually see a clear reflected symmetry between these two subfigures.

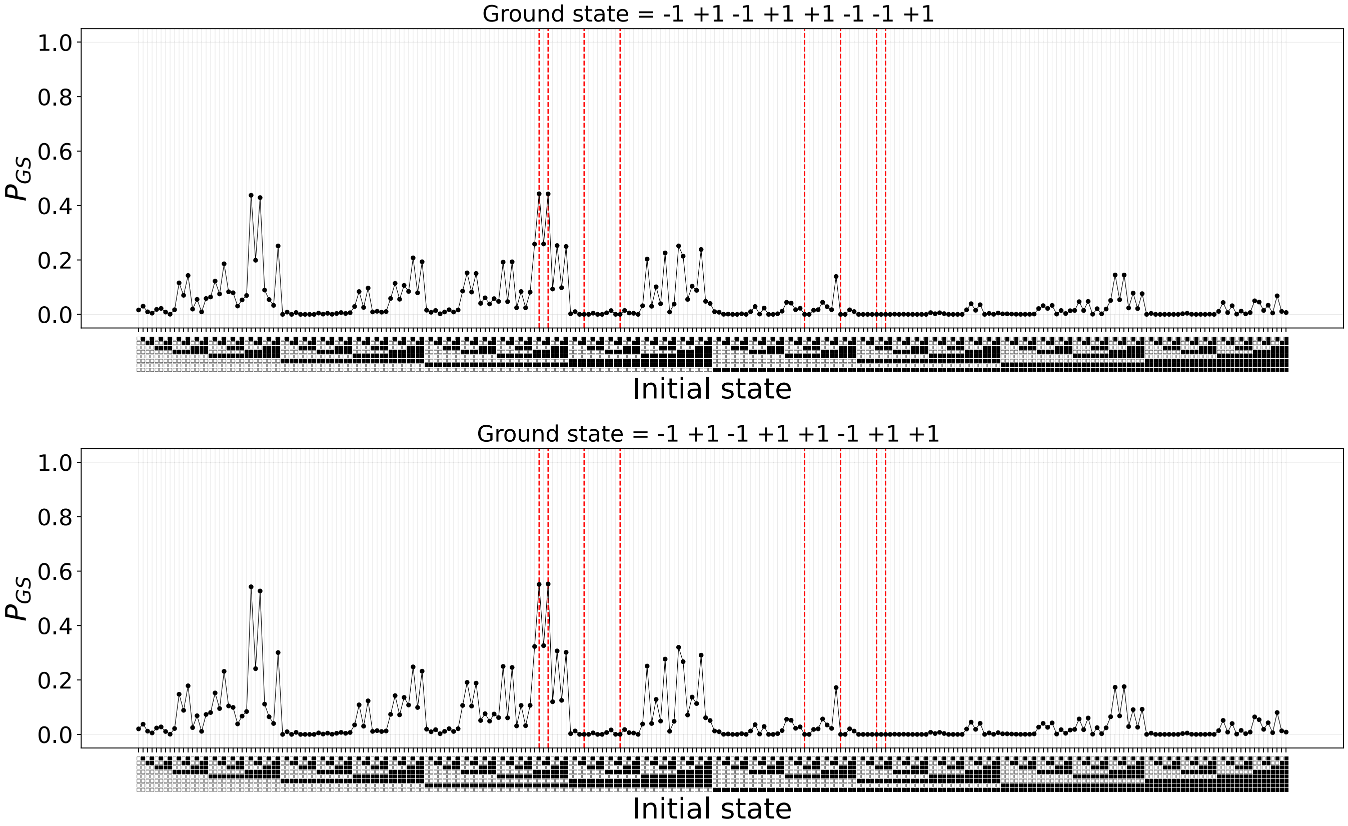

FIG. 20. Ground-state success probability for reverse annealing only, applied on the N_8 Ising. These two plots correspond to two out of the eight ground states of the N_8 Ising; the plots for the other six ground states are given in Fig. 24 in Appendix. The x-axis encodes the RA initial states as vectors of vertical blocks, where ■ denotes a variable state of $+1$ and □ denotes a variable state of -1. The initial state vectors are read from bottom to top, where the bottom is the first index which corresponds to variable 0 in the problem Ising. The initial states which are also other ground states are marked with dashed red vertical lines.

There are several open research questions that can be investigated:

(i) The observation that it requires less h-gain strength to flip high degree variables into a neighboring ground state, which lead to the creation of the δ metric, could be further evaluated for Ising models of a comparable number of variables but which have uniform variable degrees in their graph. In particular, following the observations made in this article, it would be expected that Ising models with uniform degrees would have more uniform χ across all input states.

(ii) What are the quantum annealing dynamics when forcing the system into a ground state during normal forward annealing? This can be accomplished by specifying the ground state using linear terms and an h-gain schedule that gradually increases from 0 up to some specified strength. This could allow for a determination as to whether some ground states have a higher susceptibility than others under the

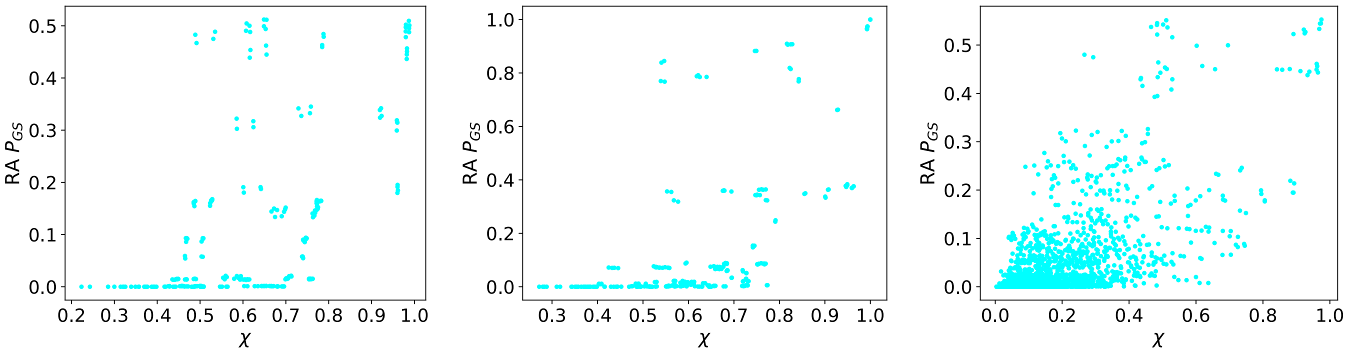

FIG. 21. Scatterplots of χ (x-axis) vs reverse annealing P_{GS} (y-axis) for each of the three Ising models. N_6 Ising (left) with a Pearson correlation coefficient of 0.553, N_7 Ising (middle) with a Pearson correlation coefficient of 0.575, and N_8 Ising (right) with a Pearson correlation coefficient of 0.648.

D-Wave implementation of the transverse field Ising model of quantum annealing, and if this correlates with the unfair sampling of ground states.

(iii) To what extent can the reverse annealing and h-gain state-to-state mapping presented in this article be applied for mapping to states that are not ground states? In principle, if the h-gain field is applied continuously over the duration of the anneal and the state freezes out before the effect of the h-gain field subsides or is intentionally reduced, then the anneal could remain in a non-ground-state at readout. If this could be implemented, a full Markov transition matrix for every classical state to every other classical state, having been passed through a quantum annealer, could be developed (including which intermediate states are found during the transition from one state to another).

(iv) The results presented in this article can be expanded to include other anneal fractions to pause the anneal at, more complex reverse annealing schedules, or more complex h-gain schedules.

(v) D-Wave Advantage_system4.1 has a maximum h-gain schedule strength of 3, but other D-Wave quantum annealers have other allowed maximum h-gain schedule values (for example, Advantage_system6.1 allows up to an h-gain schedule strength of 4). Utilizing stronger h-gain schedule amplifications could facilitate finding higher success proportions for getting the anneal into an intended ground state, in particular for the N_8 Ising.

(vi) The h-gain field can also be programed to have a *negative* bias, as opposed to a positive bias. Applying both the negative and positive h-gain fields to state mapping or phase transition experiments could be useful for the purpose of determining if there is an asymmetry in the responses to the applied h-gain field.

(vii) Unlike reverse annealing, which requires all active qubits to have an initial state specified, the h-gain state encoding method allows selective encoding of an initial state for some subset of the qubits being used for a problem Ising. Therefore, in a slightly different context than what is described in this paper, the h-gain state encoding method could be used for methods where selective variable encoding is important. For example, this could allow one to encode the states of weak or strong variable persistences of an optimization problem [135–137], which can be efficiently computed classically and describe the state of variables which always take this state in optimum solutions (strong persistences) or variables which take a specific state in at least one optimum solution if there are multiple optimal solutions (weak persistences).

(viii) These systems are small enough that quantum annealing simulators could be applied to compare with the experimental results. The limitation is that such a simulator would need to include both a reverse annealing schedule and an h-gain schedule capability.

ACKNOWLEDGMENTS

The author thanks Carleton Coffrin and Stephan Eidenbenz for providing feedback on the experimental results and versions of the manuscript at various stages of the research. The author thanks Denny Dahl for discussions on the h-gain feature, which eventually led to this idea. This work was supported by the U.S. Department of Energy through the Los Alamos National Laboratory. Los Alamos National Laboratory is operated by Triad National Security, LLC, for the National Nuclear Security Administration of U.S. Department of Energy (Contract No. 89233218CNA000001). The research presented in this article was supported by the Laboratory Directed Research and Development program. This research used resources provided by the Los Alamos National Laboratory Institutional Computing Program. This work has been assigned the technical report number LA-UR-22-31301.

APPENDIX: ADDITIONAL FIGURES

Figures 22–24 present additional plots that extend Figs. 11, 12, and 20.

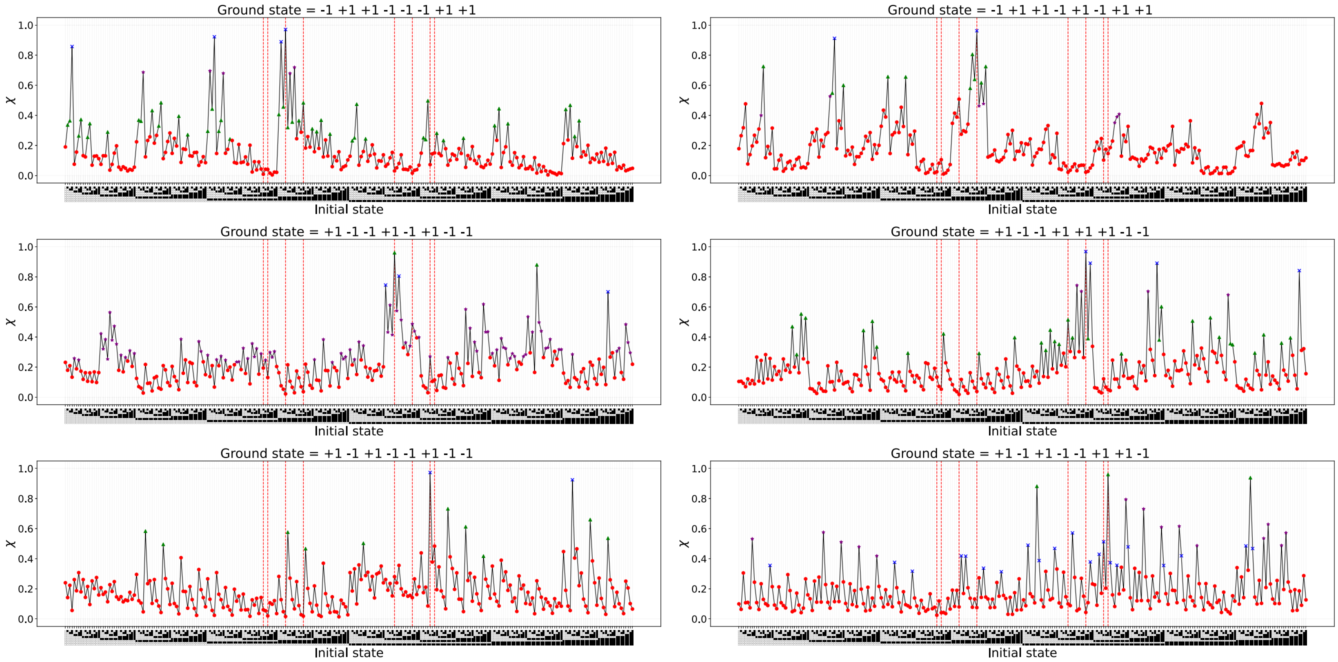

FIG. 22. These plots extend Fig. 11 with the other six ground states. The x-axis encodes the initial states as vectors of vertical blocks, where ■ denotes a variable state of $+1$ and □ denotes a variable state of -1. The initial state vectors are read from bottom to top, where the bottom is the first index which corresponds to variable 0 in the problem Ising. The initial states which are also other ground states are marked with dashed red vertical lines. For each subfigure, the reflexive ground-state mapping (i.e., where the initial state and the intended state are the same ground state) case can be found visually as the state marked with a red vertical dashed line, which has the maximum susceptibility among all of the initial states. Although this plot is considerably more dense compared to Figs. 5 and 8 because of the increase in initial states (256) and the increase in ground states (8), there are symmetries that can be clearly identified. In particular, complementary ground states show some symmetries which can be identified by the h-gain response curve clustering coloring scheme. For example, the top left subfigure and the middle right subfigure represent complementary ground states, and these plots have a symmetry across the vertical midline of each figure; the lowest susceptibility states in these two plots are complements of each other (blue colored nodes in the top left subfigure and green colored nodes in the bottom right subfigure).

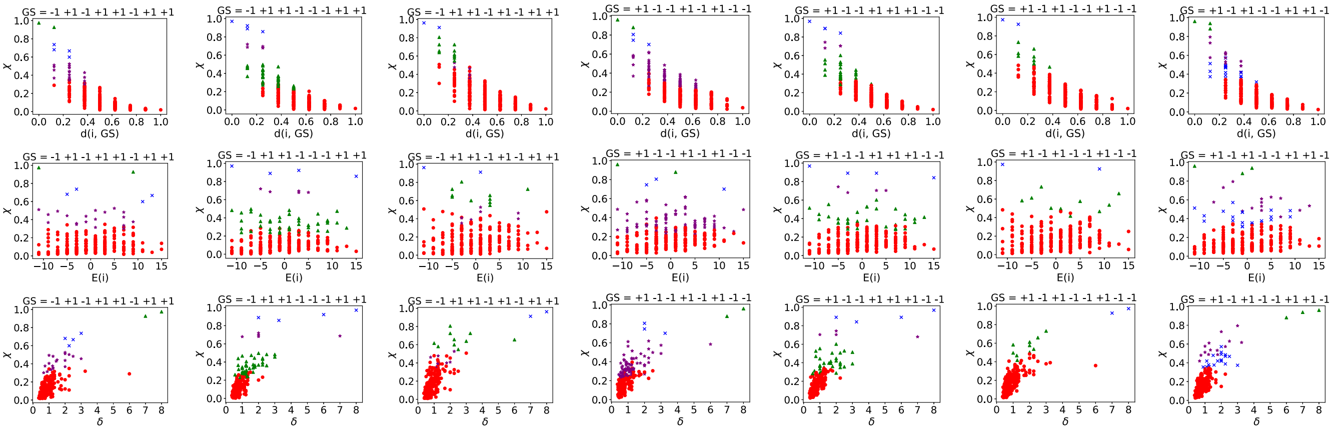

FIG. 23. The rest of the data that complete Fig. 12 with the other seven ground-state mappings. Summary metric plots for the N_8 Ising. The seven columns correspond to each of the eight ground states; the titles of each subplot are the exact optimal solution vectors. The three rows correspond to three different initial state metrics on the x-axis; the y-axis of each subplot is χ. The first row has the x-axis that is the hamming distance between the ground state and the specific initial state i. The second row has the x-axis showing the energy of the initial state i evaluated on the N_8 Ising. The third row has the x-axis showing the δ metric for each initial state.

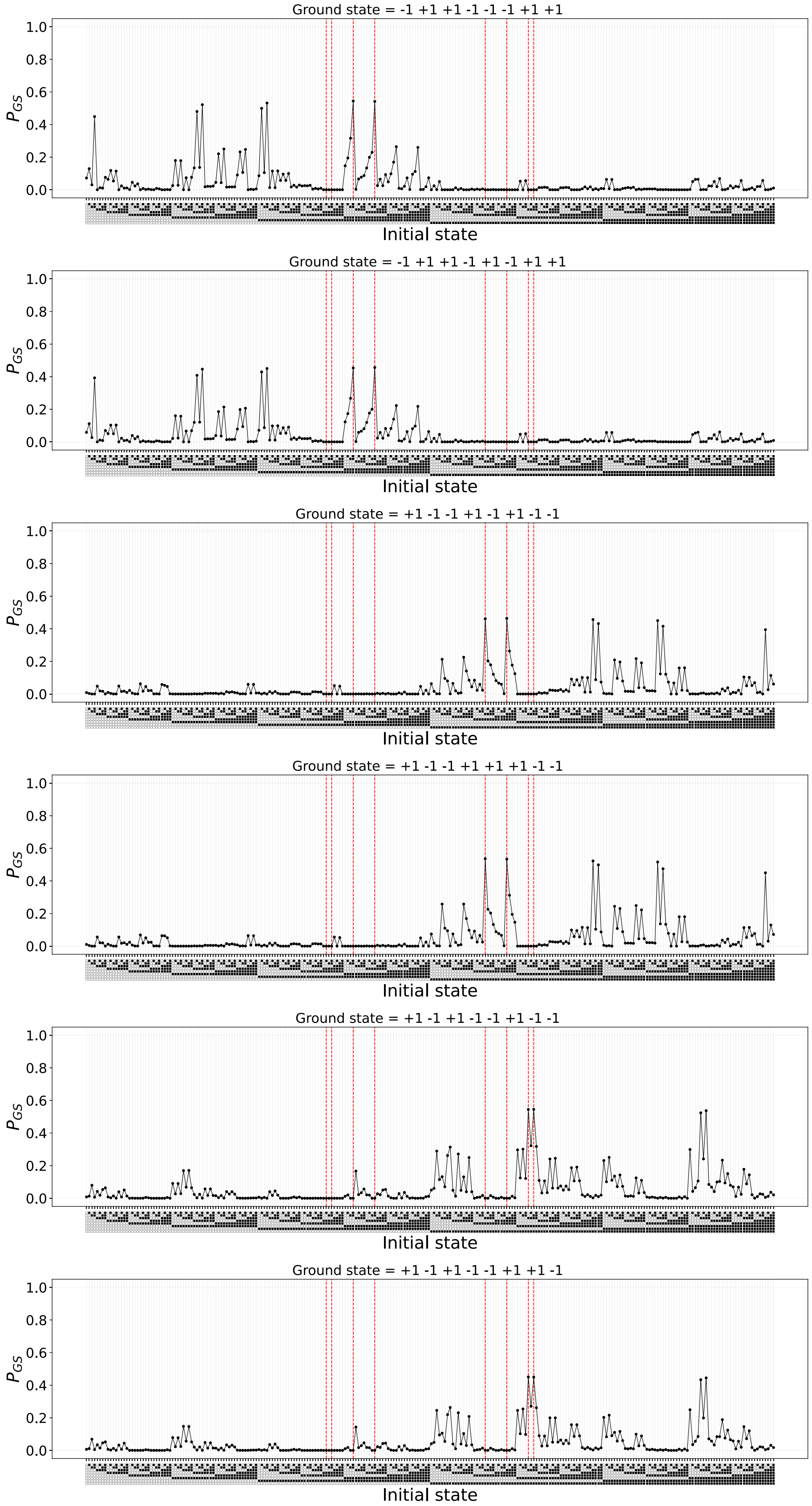
Ground state = -1 +1 +1 -1 -1 -1 +1 +1

Ground state = -1 +1 +1 -1 +1 -1 +1 +1

Ground state = +1 -1 -1 +1 -1 +1 -1 -1

Ground state = +1 -1 -1 +1 +1 +1 -1 -1

Ground state = +1 -1 +1 -1 -1 +1 -1 -1

Ground state = +1 -1 +1 -1 -1 +1 +1 -1

FIG. 24. Continuation of Fig. 20 showing the reverse-annealing-only ground-state success proportions for the other six ground states of the N_8 Ising. In each plot, all states on the x-axis that are ground states are marked with vertical dashed red lines.

[1] J. Brooke, D. Bitko, T. F. Rosenbaum, and G. Aeppli, Quantum annealing of a disordered magnet, Science **284**, 779 (1999).
[2] T. Kadowaki and H. Nishimori, Quantum annealing in the transverse Ising model, Phys. Rev. E **58**, 5355 (1998).
[3] S. Morita and H. Nishimori, Mathematical foundation of quantum annealing, J. Math. Phys. **49**, 125210 (2008).
[4] A. Das and B. K. Chakrabarti, Colloquium: Quantum annealing and analog quantum computation, Rev. Mod. Phys. **80**, 1061 (2008).
[5] A. B. Finnila, M. Gomez, C. Sebenik, C. Stenson, and J. D. Doll, Quantum annealing: A new method for minimizing multidimensional functions, Chem. Phys. Lett. **219**, 343 (1994).
[6] G. E. Santoro and E. Tosatti, Optimization using quantum mechanics: quantum annealing through adiabatic evolution, J. Phys. A **39**, R393 (2006).
[7] E. K. Grant and T. S. Humble, Adiabatic quantum computing and quantum annealing, in *Oxford Research Encyclopedia of Physics* (Oxford University Press, Oxford, 2020).
[8] P. Hauke, H. G. Katzgraber, W. Lechner, H. Nishimori, and W. D. Oliver, Perspectives of quantum annealing: Methods and implementations, Rep. Prog. Phys. **83**, 054401 (2020).
[9] M. W. Johnson, M. H. Amin, S. Gildert, T. Lanting, F. Hamze, N. Dickson, R. Harris, A. J. Berkley, J. Johansson, P. Bunyk *et al.*, Quantum annealing with manufactured spins, Nature (London) **473**, 194 (2011).
[10] S. Boixo, T. F. Rønnow, S. V. Isakov, Z. Wang, D. Wecker, D. A. Lidar, J. M. Martinis, and M. Troyer, Evidence for quantum annealing with more than one hundred qubits, Nat. Phys. **10**, 218 (2014).
[11] S. Boixo, T. Albash, F. M. Spedalieri, N. Chancellor, and D. A. Lidar, Experimental signature of programmable quantum annealing, Nat. Commun. **4**, 2067 (2013).
[12] R. Harris, Y. Sato, A. Berkley, M. Reis, F. Altomare, M. Amin, K. Boothby, P. Bunyk, C. Deng, C. Enderud *et al.*, Phase transitions in a programmable quantum spin glass simulator, Science **361**, 162 (2018).
[13] A. D. King, C. Nisoli, E. D. Dahl, G. Poulin-Lamarre, and A. Lopez-Bezanilla, Qubit spin ice, Science **373**, 576 (2021).
[14] S. Zhou, D. Green, E. D. Dahl, and C. Chamon, Experimental realization of classical $\mathbb{Z}_2$ spin liquids in a programmable quantum device, Phys. Rev. B **104**, L081107 (2021).
[15] A. D. King, J. Raymond, T. Lanting, S. V. Isakov, M. Mohseni, G. Poulin-Lamarre, S. Ejtemaee, W. Bernoudy, I. Ozfidan, A. Y. Smirnov *et al.*, Scaling advantage over path-integral Monte Carlo in quantum simulation of geometrically frustrated magnets, Nat. Commun. **12**, 1 (2021).
[16] H. Munoz-Bauza, H. Chen, and D. Lidar, A double-slit proposal for quantum annealing, npj Quantum Inf. **5**, 51 (2019).
[17] C. C. McGeoch and C. Wang, in *Proceedings of the ACM International Conference on Computing Frontiers*, CF '13 (Association for Computing Machinery, New York, 2013).
[18] D. Vert, R. Sirdey, and S. Louise, Benchmarking quantum annealing against "hard" instances of the bipartite matching problem, SN Comput. Sci. **2**, 106 (2021).
[19] S. Yarkoni, E. Raponi, T. Bäck, and S. Schmitt, Quantum annealing for industry applications: Introduction and review, Rep. Prog. Phys. **85**, 104001 (2022).
[20] E. Boyda, S. Basu, S. Ganguly, A. Michaelis, S. Mukhopadhyay, and R. R. Nemani, Deploying a quantum annealing processor to detect tree cover in aerial imagery of california, PLoS ONE **12**, e0172505 (2017).
[21] O. Titiloye and A. Crispin, Quantum annealing of the graph coloring problem, Discrete Optimization **8**, 376 (2011).
[22] J. Kwok and K. Pudenz, Graph coloring with quantum annealing, arXiv:2012.04470.
[23] S. Jiang, K. A. Britt, A. J. McCaskey, T. S. Humble, and S. Kais, Quantum annealing for prime factorization, Sci. Rep. **8**, 17667 (2018).
[24] R. Dridi and H. Alghassi, Prime factorization using quantum annealing and computational algebraic geometry, Sci. Rep. **7**, 43048 (2017).
[25] W. Peng, B. Wang, F. Hu, Y. Wang, X. Fang, X. Chen, and C. Wang, Factoring larger integers with fewer qubits via quantum annealing with optimized parameters, Sci. China Phys. Mech. Astron. **62**, 60311 (2019).
[26] R. H. Warren, Factoring on a quantum annealing computer, Quantum Inf. Comput. **19**, 252 (2019).
[27] M. Wroński, Practical solving of discrete logarithm problem over prime fields using quantum annealing, Cryptology ePrint Archive, Paper 2021/527 (2021).
[28] R. Mengoni, D. Ottaviani, and P. Iorio, Breaking RSA security with a low noise D-wave 2000Q quantum annealer: Computational times, limitations and prospects, arXiv:2005.02268.
[29] C. Silva, A. Aguiar, P. Lima, and I. Dutra, Mapping a logical representation of TSP to quantum annealing, Quant. Inf. Proc. **20**, 386 (2021).
[30] C. Papalitsas, T. Andronikos, K. Giannakis, G. Theocharopoulou, and S. Fanarioti, A QUBO model for the traveling salesman problem with time windows, Algorithms **12**, 224 (2019).
[31] T. Stollenwerk, B. O'Gorman, D. Venturelli, S. Mandra, O. Rodionova, H. Ng, B. Sridhar, E. G. Rieffel, and R. Biswas, Quantum annealing applied to de-conflicting optimal trajectories for air traffic management, IEEE Trans. Intell. Transport. Syst. **21**, 285 (2019).
[32] E. Pelofske, G. Hahn, and H. N. Djidjev, Parallel quantum annealing, Sci. Rep. **12**, 4499 (2022).
[33] G. Chapuis, H. Djidjev, G. Hahn, and G. Rizk, Finding maximum cliques on the d-wave quantum annealer, J. Sign. Proc. Syst. **91**, 363 (2019).
[34] E. Pelofske, G. Hahn, and H. Djidjev, Solving large minimum vertex cover problems on a quantum annealer, in *Proceedings of the 16th ACM International Conference on Computing Frontiers*, CF'19 (ACM, New York, 2019), pp. 76–84.
[35] H. Ushijima-Mwesigwa, C. F. Negre, and S. M. Mniszewski, Graph partitioning using quantum annealing on the D-wave system, in *Proceedings of the Second International Workshop on Post Moores Era Supercomputing*, PMES'17 (ACM, New York, 2017), pp. 22–29.
[36] E. Pelofske, G. Hahn, and H. N. Djidjev, in *Proceedings of the 18th ACM International Conference on Computing Frontiers*, CF '21 (Association for Computing Machinery, New York, 2021), pp. 133–139.
[37] D. O'Malley, H. N. Djidjev, and B. S. Alexandrov, in *2020 International Conference on Rebooting Computing (ICRC)* (IEEE, Piscataway, NJ, 2020), pp. 58–65.
[38] E. Pelofske, G. Hahn, D. O'Malley, H. N. Djidjev, and B. S. Alexandrov, Boolean hierarchical tucker networks on quantum annealers, in *Large-Scale Scientific Computing*, edited by

I. Lirkov (Springer International Publishing, Cham, 2022), pp. 351–358.

[39] E. Pelofske, G. Hahn, D. O'Malley, H. N. Djidjev, and B. S. Alexandrov, Quantum annealing algorithms for Boolean tensor networks, Sci. Rep. **12**, 8539 (2022).

[40] C. F. Negre, H. Ushijima-Mwesigwa, and S. M. Mniszewski, Detecting multiple communities using quantum annealing on the D-wave system, PLoS ONE **15**, e0227538 (2020).

[41] M. Novotny, Q. L. Hobl, J. Hall, and K. Michielsen, Spanning tree calculations on D-wave 2 machines, J. Phys.: Conf. Ser. **681**, 012005 (2016).

[42] A. Perdomo-Ortiz, J. Fluegemann, S. Narasimhan, R. Biswas, and V. N. Smelyanskiy, A quantum annealing approach for fault detection and diagnosis of graph-based systems, Eur. Phys. J.: Spec. Top. **224**, 131 (2015).

[43] E. Pelofske, G. Hahn, and H. N. Djidjev, in *2020 IEEE International Conference on Quantum Computing and Engineering (QCE)* (IEEE, Piscataway, NJ, 2020), pp. 256–266.

[44] A. Barbosa, E. Pelofske, G. Hahn, and H. N. Djidjev, Optimizing embedding-related quantum annealing parameters for reducing hardware bias, in *Parallel Architectures, Algorithms and Programming* (Springer, Singapore, 2021), pp. 162–173.

[45] J. Berwald, N. Chancellor, and R. Dridi, Understanding domain-wall encoding theoretically and experimentally, Phil. Trans. R. Soc. A **381**, 20210410 (2023).

[46] J. Chen, T. Stollenwerk, and N. Chancellor, Performance of domain-wall encoding for quantum annealing, IEEE Trans. Quantum Eng. **2**, 1 (2021).

[47] N. Chancellor, Domain wall encoding of discrete variables for quantum annealing and QAOA, Quantum Sci. Technol. **4**, 045004 (2019).

[48] M. Khezri, X. Dai, R. Yang, T. Albash, A. Lupascu, and D. A. Lidar, Customized Quantum Annealing Schedules, Phys. Rev. Appl. **17**, 044005 (2022).

[49] A. Mishra, T. Albash, and D. A. Lidar, Performance of two different quantum annealing correction codes, Quant. Inf. Proc. **15**, 609 (2016).

[50] K. L. Pudenz, T. Albash, and D. A. Lidar, Quantum annealing correction for random Ising problems, Phys. Rev. A **91**, 042302 (2015).

[51] W. Vinci, T. Albash, G. Paz-Silva, I. Hen, and D. A. Lidar, Quantum annealing correction with minor embedding, Phys. Rev. A **92**, 042310 (2015).

[52] J. Preskill, Quantum computing in the NISQ era and beyond, Quantum **2**, 79 (2018).

[53] M. S. Könz, W. Lechner, H. G. Katzgraber, and M. Troyer, Embedding overhead scaling of optimization problems in quantum annealing, PRX Quantum **2**, 040322 (2021).

[54] T. Boothby, A. D. King, and A. Roy, Fast clique minor generation in Chimera qubit connectivity graphs, Quant. Inf. Proc. **15**, 495 (2016).

[55] K. Boothby, P. Bunyk, J. Raymond, and A. Roy, Next-generation topology of d-wave quantum processors, arXiv:2003.00133.

[56] E. Farhi, J. Goldstone, S. Gutmann, and M. Sipser, Quantum computation by adiabatic evolution, arXiv:quant-ph/0001106.

[57] A. Lucas, Ising formulations of many NP problems, Front. Phys. **2**, 5 (2014).

[58] F. Glover, G. Kochenberger, and Y. Du, A tutorial on formulating and using QUBO models, arXiv:1811.11538.

[59] M. Zaman, K. Tanahashi, and S. Tanaka, PyQUBO: Python library for mapping combinatorial optimization problems to QUBO form, IEEE Trans. Comput. **71**, 838 (2021).

[60] S. Abel and M. Spannowsky, Quantum-field-theoretic simulation platform for observing the fate of the false vacuum, PRX Quantum **2**, 010349 (2021).

[61] S. Abel, N. Chancellor, and M. Spannowsky, Quantum computing for quantum tunneling, Phys. Rev. D **103**, 016008 (2021).

[62] D. T. O'Connor, L. Fry-Bouriaux, and P. A. Warburton, Perturbed ferromagnetic chain: Tunable test of hardness in the transverse-field Ising model, Phys. Rev. A **105**, 022410 (2022).

[63] E. Pelofske, G. Hahn, and H. Djidjev, Inferring the dynamics of the state evolution during quantum annealing, IEEE Trans. Parallel Distrib. Syst. **33**, 310 (2020).

[64] E. Pelofske, G. Hahn, and H. Djidjev, Peering into the anneal process of a quantum annealer, in *2019 20th International Conference on Parallel and Distributed Computing, Applications and Technologies (PDCAT)* (IEEE, Piscataway, NJ, 2019), pp. 184–189.

[65] Y. Matsuda, H. Nishimori, and H. G. Katzgraber, Ground-state statistics from annealing algorithms: quantum versus classical approaches, New J. Phys. **11**, 073021 (2009).

[66] E. Pelofske, J. Golden, A. Bärtschi, D. O'Malley, and S. Eidenbenz, Sampling on NISQ Devices: "Who's the Fairest One of All?," in *2021 IEEE International Conference on Quantum Computing and Engineering (QCE)* (IEEE, Piscataway, NJ, 2021), pp. 207–217.

[67] M. S. Könz, G. Mazzola, A. J. Ochoa, H. G. Katzgraber, and M. Troyer, Uncertain fate of fair sampling in quantum annealing, Phys. Rev. A **100**, 030303(R) (2019).

[68] V. Kumar, C. Tomlin, C. Nehrkorn, D. O'Malley, and J. Dulny III, Achieving fair sampling in quantum annealing, arXiv:2007.08487.

[69] S. Mandrà, Z. Zhu, and H. G. Katzgraber, Exponentially Biased Ground-State Sampling of Quantum Annealing Machines with Transverse-Field Driving Hamiltonians, Phys. Rev. Lett. **118**, 070502 (2017).

[70] M. Yamamoto, M. Ohzeki, and K. Tanaka, Fair sampling by simulated annealing on quantum annealer, J. Phys. Soc. Jpn. **89**, 025002 (2020).

[71] Z. Zhu, A. J. Ochoa, and H. G. Katzgraber, Fair sampling of ground-state configurations of binary optimization problems, Phys. Rev. E **99**, 063314 (2019).

[72] A. J. Ochoa, D. C. Jacob, S. Mandrà, and H. G. Katzgraber, Feeding the multitude: A polynomial-time algorithm to improve sampling, Phys. Rev. E **99**, 043306 (2019).

[73] S. Eslami, N. Heess, C. K. Williams, and J. Winn, The shape Boltzmann machine: A strong model of object shape, Int. J. Comput. Vision **107**, 155 (2014).

[74] G. E. Hinton, Training products of experts by minimizing contrastive divergence, Neural Comput. **14**, 1771 (2002).

[75] C. P. Gomes, A. Sabharwal, and B. Selman, in *Handbook of Satisfiability* (IOS Press, 2021), pp. 993–1014.

[76] M. R. Jerrum, L. G. Valiant, and V. V. Vazirani, Random generation of combinatorial structures from a uniform distribution, Theor. Comput. Sci. **43**, 169 (1986).

[77] M. Azinović, D. Herr, B. Heim, E. Brown, and M. Troyer, Assessment of quantum annealing for the construction of satisfiability filters, SciPost Phys. **2**, 013 (2017).

[78] A. Douglass, A. D. King, and J. Raymond, Constructing SAT filters with a quantum annealer, in *Theory and Applications of Satisfiability Testing – SAT 2015*, Lecture Notes in Computer Science, Vol. 9340 (Springer, Cham, 2015), pp. 104–120.

[79] S. A. Weaver, K. J. Ray, V. W. Marek, A. J. Mayer, and A. K. Walker, Satisfiability-based set membership filters, J. Satisfiability, Boolean Modeling Computat. **8**, 129 (2012).

[80] T. J. Schaefer, The complexity of satisfiability problems, in *Proceedings of the Tenth Annual ACM Symposium on Theory of Computing*, STOC '78 (Association for Computing Machinery, New York, 1978), pp. 216–226.

[81] Y. Mizuno and T. Komatsuzaki, A note on enumeration by fair sampling, arXiv:2104.01941.

[82] E. Pelofske, Dataset for mapping state transition susceptibility in quantum annealing Part 1, Zenodo (2023), https://doi.org/10.5281/zenodo.7676291.

[83] E. Pelofske, Dataset for mapping state transition susceptibility in quantum annealing Part 2, Zenodo (2023), https://doi.org/10.5281/zenodo.7676350.

[84] E. Pelofske, Dataset for mapping state transition susceptibility in quantum annealing Part 3, Zenodo (2023), https://doi.org/10.5281/zenodo.7676389.

[85] E. Pelofske, Dataset for mapping state transition susceptibility in quantum annealing Part 4, Zenodo (2023), https://doi.org/10.5281/zenodo.7677424.

[86] J. D. Hunter, Matplotlib: A 2D graphics environment, Comput. Sci. Eng. **9**, 90 (2007).

[87] T. A. Caswell, M. Droettboom, A. Lee, E. S. de Andrade, T. Hoffmann, J. Klymak, J. Hunter, E. Firing, D. Stansby, N. Varoquaux, J. H. Nielsen, B. Root, R. May, P. Elson, J. K. Seppänen, D. Dale, J.-J. Lee, D. McDougall, A. Straw, P. Hobson *et al.*, matplotlib/matplotlib: Rel: v3.5.2 (2022).

[88] A. Hagberg, P. Swart, and D. S Chult, Exploring network structure, dynamics, and function using NetworkX, Tech. Rep. No. LA-UR-08-05495 (Los Alamos National Lab, Los Alamos, NM, 2008), https://www.osti.gov/biblio/960616.

[89] N. Dattani, S. Szalay, and N. Chancellor, Pegasus: The second connectivity graph for large-scale quantum annealing hardware, arXiv:1901.07636.

[90] S. Zbinden, A. Bärtschi, H. Djidjev, and S. Eidenbenz, in *International Conference on High Performance Computing* (Springer, Berlin, Heidelberg, 2020), pp. 187–206.

[91] https://dwave-systemdocs.readthedocs.io/en/samplers/reference/composites/tiling.html.

[92] J. Marshall, G. Mossi, and E. G. Rieffel, Perils of embedding for quantum sampling, Phys. Rev. A **105**, 022615 (2022).

[93] E. Grant and T. S. Humble, Benchmarking embedded chain breaking in quantum annealing, Quantum Sci. Technol. **7**, 025029 (2022).

[94] C. J. Coffrin, Challenges with chains: Testing the limits of a D-wave quantum annealer for discrete optimization, doi:10.2172/1498001 (2019).

[95] J. Cai, W. G. Macready, and A. Roy, A practical heuristic for finding graph minors, arXiv:1406.2741.

[96] D. Venturelli, S. Mandrà, S. Knysh, B. O'Gorman, R. Biswas, and V. Smelyanskiy, Quantum Optimization of Fully Connected Spin Glasses, Phys. Rev. X **5**, 031040 (2015).

[97] J. Raymond, R. Stevanovic, W. Bernoudy, K. Boothby, C. McGeoch, A. J. Berkley, P. Farré, and A. D. King, Hybrid quantum annealing for larger-than-QPU lattice-structured problems, in *ACM Transactions on Quantum Computing* (Association for Computing Machinery, New York, 2023).

[98] L. Hormozi, E. W. Brown, G. Carleo, and M. Troyer, Nonstoquastic Hamiltonians and quantum annealing of an Ising spin glass, Phys. Rev. B **95**, 184416 (2017).

[99] F. Barahona, On the computational complexity of Ising spin glass models, J. Phys. A **15**, 3241 (1982).

[100] A. D. King, C. D. Batista, J. Raymond, T. Lanting, I. Ozfidan, G. Poulin-Lamarre, H. Zhang, and M. H. Amin, Quantum annealing simulation of out-of-equilibrium magnetization in a spin-chain compound, PRX Quantum **2**, 030317 (2021).

[101] Z. Morrell, M. Vuffray, A. Lokhov, A. Bärtschi, T. Albash, and C. Coffrin, Signatures of Open and Noisy Quantum Systems in Single-Qubit Quantum Annealing, Phys. Rev. Appl. **19**, 034053 (2023).

[102] G. Passarelli, K.-W. Yip, D. A. Lidar, and P. Lucignano, Standard quantum annealing outperforms adiabatic reverse annealing with decoherence, Phys. Rev. A **105**, 032431 (2022).

[103] Y. Yamashiro, M. Ohkuwa, H. Nishimori, and D. A. Lidar, Dynamics of reverse annealing for the fully connected p-spin model, Phys. Rev. A **100**, 052321 (2019).

[104] M. Ohkuwa, H. Nishimori, and D. A. Lidar, Reverse annealing for the fully connected p-spin model, Phys. Rev. A **98**, 022314 (2018).

[105] J. Golden and D. O'Malley, Reverse annealing for nonnegative/binary matrix factorization, PLoS ONE **16**, e0244026 (2021).

[106] D. Venturelli and A. Kondratyev, Reverse quantum annealing approach to portfolio optimization problems, Quantum Machine Intell. **1**, 17 (2019).

[107] A. Perdomo-Ortiz, S. E. Venegas-Andraca, and A. Aspuru-Guzik, A study of heuristic guesses for adiabatic quantum computation, Quant. Inf. Proc. **10**, 33 (2011).

[108] N. Chancellor, Modernizing quantum annealing using local searches, New J. Phys. **19**, 023024 (2017).

[109] J. Marshall, D. Venturelli, I. Hen, and E. G. Rieffel, Power of Pausing: Advancing Understanding of Thermalization in Experimental Quantum Annealers, Phys. Rev. Appl. **11**, 044083 (2019).

[110] H. G. Katzgraber, F. Hamze, and R. S. Andrist, Glassy Chimeras Could Be Blind to Quantum Speedup: Designing Better Benchmarks for Quantum Annealing Machines, Phys. Rev. X **4**, 021008 (2014).

[111] F. Pedregosa, G. Varoquaux, A. Gramfort, V. Michel, B. Thirion, O. Grisel, M. Blondel, P. Prettenhofer, R. Weiss, V. Dubourg, J. Vanderplas, A. Passos, D. Cournapeau, M. Brucher, M. Perrot, and E. Duchesnay, Scikit-learn: Machine learning in Python, J. Machine Learning Res. **12**, 2825 (2011).

[112] L. Buitinck, G. Louppe, M. Blondel, F. Pedregosa, A. Mueller, O. Grisel, V. Niculae, P. Prettenhofer, A. Gramfort, J. Grobler, R. Layton, J. VanderPlas, A. Joly, B. Holt, and G. Varoquaux, API design for machine learning software experiences from the scikit-learn project, arXiv:1309.0238.

[113] A. Damle, V. Minden, and L. Ying, Simple, direct and efficient multi-way spectral clustering, Inf. Infer.: J. IMA **8**, 181 (2019).

[114] A. V. Knyazev, Toward the optimal preconditioned eigensolver: Locally optimal block preconditioned conjugate gradient method, SIAM J. Sci. Comput. **23**, 517 (2001).

[115] X. Y. Stella and J. Shi, in *Proceedings of the Ninth IEEE International Conference on Computer Vision* (IEEE, Piscataway, NJ, 2003), Vol. 1, pp. 313–319.

[116] U. von Luxburg, A tutorial on spectral clustering, Stat. Comput. **17**, 395 (2007).

[117] J. Jianbo Shi and J. Malik, Normalized cuts and image segmentation, IEEE Trans. Pattern Anal. Machine Intell. **22**, 888 (2000).

[118] T. M. Fruchterman and E. M. Reingold, Graph drawing by force-directed placement, Softw: Pract. Exper. **21**, 1129 (1991).

[119] P. Virtanen, R. Gommers, T. E. Oliphant, M. Haberland, T. Reddy, D. Cournapeau, E. Burovski, P. Peterson, W. Weckesser, J. Bright, S. J. van der Walt, M. Brett, J. Wilson, K. J. Millman, N. Mayorov, A. R. J. Nelson, E. Jones, R. Kern, E. Larson, C. J. Carey *et al.*, SciPy 1.0: Fundamental Algorithms for Scientific Computing in Python, Nat. Methods **17**, 261 (2020).

[120] M. Kowalsky, T. Albash, I. Hen, and D. A. Lidar, 3-regular three-XORSAT planted solutions benchmark of classical and quantum heuristic optimizers, Quantum Sci. Technol. **7**, 025008 (2022).

[121] I. Hen, J. Job, T. Albash, T. F. Rønnow, M. Troyer, and D. A. Lidar, Probing for quantum speedup in spin-glass problems with planted solutions, Phys. Rev. A **92**, 042325 (2015).

[122] D. Perera, F. Hamze, J. Raymond, M. Weigel, and H. G. Katzgraber, Computational hardness of spin-glass problems with tile-planted solutions, Phys. Rev. E **101**, 023316 (2020).

[123] J. Raymond, R. Stevanovic, W. Bernoudy, K. Boothby, C. McGeoch, A. J. Berkley, P. Farré, and A. D. King, Hybrid quantum annealing for larger-than-QPU lattice-structured problems, arXiv:2202.03044.

[124] D. Perera, I. Akpabio, F. Hamze, S. Mandra, N. Rose, M. Aramon, and H. G. Katzgraber, Chook - A comprehensive suite for generating binary optimization problems with planted solutions, arXiv:2005.14344.

[125] Y. Pang, C. Coffrin, A. Y. Lokhov, and M. Vuffray, The potential of quantum annealing for rapid solution structure identification, in *Integration of Constraint Programming, Artificial Intelligence, and Operations Research*, edited by E. Hebrard and N. Musliu (Springer International Publishing, 2020).

[126] T. Albash and D. A. Lidar, Demonstration of a Scaling Advantage for a Quantum Annealer Over Simulated Annealing, Phys. Rev. X **8**, 031016 (2018).

[127] V. S. Denchev, S. Boixo, S. V. Isakov, N. Ding, R. Babbush, V. Smelyanskiy, J. Martinis, and H. Neven, What is the Computational Value of Finite-Range Tunneling?, Phys. Rev. X **6**, 031015 (2016).

[128] J. King, S. Yarkoni, J. Raymond, I. Ozfidan, A. D. King, M. M. Nevisi, J. P. Hilton, and C. C. McGeoch, Quantum annealing amid local ruggedness and global frustration, J. Phys. Soc. Jpn. **88**, 061007 (2019).

[129] A. D. King, T. Lanting, and R. Harris, Performance of a quantum annealer on range-limited constraint satisfaction problems, arXiv:1502.02098.

[130] J. King, S. Yarkoni, M. M. Nevisi, J. P. Hilton, and C. C. McGeoch, Benchmarking a quantum annealing processor with the time-to-target metric, arXiv:1508.05087.

[131] L. Zdeborova and F. Krzakala, Statistical physics of inference: thresholds and algorithms, Adv. Phys. **65**, 453 (2016).

[132] M. Cain, E. Farhi, S. Gutmann, D. Ranard, and E. Tang, The QAOA gets stuck starting from a good classical string, arXiv:2207.05089.

[133] D. J. Egger, J. Mareček, and S. Woerner, Warm-starting quantum optimization, Quantum **5**, 479 (2021).

[134] S. Hadfield, Z. Wang, B. O'Gorman, E. Rieffel, D. Venturelli, and R. Biswas, From the quantum approximate optimization algorithm to a quantum alternating operator ansatz, Algorithms **12**, 34 (2019).

[135] P. L. Hammer, P. Hansen, and B. Simeone, Roof duality, complementation and persistency in quadratic 0–1 optimization, Math. Program. **28**, 121 (1984).

[136] A. Billionnet and A. Sutter, Persistency in quadratic 0–1 optimization, Math. Program. **54**, 115 (1992).

[137] T. Windheuser, H. Ishikawa, and D. Cremers, in *European Conference on Computer Vision* (Springer, Berlin, Heidelberg, 2012), pp. 400–413.